AIAA SciTech Forum
11–15 & 19–21 January 2021, VIRTUAL EVENT
AIAA Scitech 2021 Forum

10.2514/6.2021-1428

In-Tunnel Simulations of the NASA Juncture Flow Model

Nash'at N. Ahmad*, Christopher L. Rumsey†, Jan-Renee Carlson‡
NASA Langley Research Center, Hampton, Virginia, 23681

The effect of wind tunnel walls on the development of flow separation in the wing-fuselage juncture area is assessed using FUN3D's overset and wind tunnel controller capabilities. The simulation data obtained from the in-tunnel runs are compared with the free-air simulations. The simulation results are also evaluated using measurements from the recently completed Phase 2 of the Juncture Flow Experiment. In general, the simulation data compared well with the measurements, however there were no significant differences in the prediction of the separation location, size, and shape, between the free-air and the in-tunnel runs. The results of this study suggest that the effects of tunnel walls on the flow separation in the juncture region are relatively small.

I. Introduction

IN certain cases, the modeling of the wind tunnel walls can become necessary, e.g., if the test article is mounted directly on the tunnel wall [1] or if the test article size is relatively large in relation to the test section [2]. Although for many applications, the assumption of free-air works sufficiently well, there is always a desire to quantify the effects (if any) of the tunnel walls on the simulation results. This study focuses on the Juncture Flow (JF) Experiment [3–6], which was designed to measure the detailed flowfield in the wing-fuselage juncture area. The main objectives of the experiment were to assess the performance of currently implemented turbulence models, and to advance the state-of-the-art in turbulence modeling based on JF measurements. Computational Fluid Dynamics (CFD) models in the past have had difficulty predicting the flow separation in the wing-fuselage juncture region [7]. Solutions from different codes and turbulence schemes have shown large variations in the prediction of separation initiation location, and separation bubble topology.

The second phase of the juncture flow experiments was conducted in the NASA Langley Research Center 14- by 22-Foot Subsonic Tunnel (14x22) in the Spring of 2020 [8]. The experiment used a custom-built Laser Doppler Velocimetry (LDV) system mounted inside the fuselage to measure the flowfield in the juncture region. The LDV measured planes at selected locations, in addition to the profiles of mean velocity components, and turbulence quantities (shear and normal stresses, as well as all components of the velocity triple products). Oil flow visualization was used to provide an estimate of the separation bubble size. A large number of static pressure ports were installed on the model wing and on the fuselage. The resulting exceptionally detailed CFD validation-quality data are publicly available from NASA's Turbulence Modeling Resource (TMR) website [9]. Assessments of NASA's FUN3D [10] and OVERFLOW [11] codes based on comparisons with the Phase I Juncture Flow data are given in Rumsey et al. [12–13], Lee and Pulliam [14], and Abdol-Hamid et al. [15].

The juncture flow CFD studies so far have primarily used free-air grids, with some effort focused on quantifying the effects of tunnel walls on the flow separation in the juncture region. Rumsey et al. [13] found minor impact of tunnel walls in their simulations of the JF model using OVERFLOW. Lee and Pulliam [14] have also reported small differences in both the bubble shape and size between the free-air and in-tunnel runs on medium and fine resolution grids using OVERFLOW. They also reported slight improvements in the prediction of surface pressures on the upper surface of the wing compared to the free-air runs. Similar results were also obtained by Abdol-Hamid et al. [15] using FUN3D. The mesh used in Abdol-Hamid [15], however, was of coarse resolution and the wind tunnel grid did not have a diffuser section. The purpose of this study is to further explore the benefits of including tunnel walls by using higher resolution grids as well as the tunnel configuration with the diffuser section. In the following sections, the simulation setup using FUN3D's overset [16] and wind tunnel controller [17] capabilities is given, and the simulation results are evaluated using the JF measurements.

---

* Research Scientist, Computational Aerosciences Branch. Senior Member, AIAA.
† Research Scientist, Computational Aerosciences Branch. Fellow, AIAA.
‡ Research Scientist, Computational Aerosciences Branch. Associate Fellow, AIAA.

II. Fully Unstructured Navier-Stokes 3D (FUN3D) Code

The Fully Unstructured Navier-Stokes 3D (FUN3D) is a versatile code that has been used to solve complex flow problems ranging from hypersonics to aeroacoustics (`https://fun3d.larc.nasa.gov`) [18–19]. FUN3D is based on a node-centered, finite-volume scheme designed to compute both compressible and incompressible flows on grids with different types of elements. Several schemes are available for computing the convective fluxes. Computation of viscous fluxes on tetrahedral meshes is based on the Green-Gauss theorem and on nontetrahedral grids, an edge-derivative augmentation is employed to avoid odd-even decoupling. A number of turbulence models have been implemented in the code that range from single equation models to hybrid Reynolds-averaged Navier-Stokes/Large Eddy Simulation (RANS/LES) capability. Time integration toward a steady state is based on a backward-Euler scheme with local time-stepping to accelerate convergence [20].

III. Simulations of the Juncture Flow Model in the 14– by 22–Foot Wind Tunnel

A. Simulation Setup

The reference Reynolds number (Re_c) in the tunnel based on the crank chord was fixed at 2.4 million. The unit Reynolds number, Re_u (1/mm) is specified in the simulations, which was set to 4307.4515 based on the chord length. The 14x22 wind tunnel does not have a temperature controller and in order to maintain a constant Reynolds number, the tunnel velocity was adjusted to account for changes in the temperature. In the simulations, the reference temperature was set to 288.84 K. The Mach number in the simulations was set to 0.189. Simulations were conducted for three angles of attack (–2.5°, 5°, and 7.5°) configurations. The reference conditions and the tunnel inflow boundary conditions are given in Table 1. Dynamic boundary conditions were imposed at the outflow in the in-tunnel simulations using a proportional-integral-derivative (PID) controller [17] to adjust the back pressure based on a user-specified target parameter (e.g., the reference Reynolds number).

Table 1: Reference and Boundary Conditions.

Parameter	FUN3D
Mach Number	0.189
Unit Reynolds Number	Re_u (1/mm)=4307.4515
T_{ref}	288.84 K
Total pressure ratio	1.0252288
Total temperature ratio	1.0071442
$(\alpha_1, \alpha_2, \alpha_3)$	(–2.5°, 5°, 7.5°)

The JF model was built with a truncated DLR-F6 wing with a span of 3397.25 mm and a 27.1° leading edge sweep. The crank chord length was 557.17 mm (located at 759 mm from the fuselage). The fuselage length, height, and width were 4839 mm, 670 mm, and 472 mm, respectively. The origin of the coordinates was set at the fuselage nose and the *x*-axis ran along the fuselage centerline. The *y*-axis was in the spanwise direction (positive in the starboard direction). The LDV probes scanned the wing on the port side. The wing-fuselage juncture was at y = –236.1 mm on the port side and the wing root trailing edge was at x = 2961.9 mm.

Unstructured grids of coarse and medium resolutions were generated using VGRID [21] with approximately 11 million and 36 million nodes, respectively. A zoomed view of the wing-fuselage section for the coarse and the medium grids is shown in Figure 1. The grids were generated for a half-span JF model with symmetry boundary condition in the *x*-*z* plane. Several grids were generated for the empty 14x22 wind tunnel for different configurations (with diffuser, without diffuser, extended settling chamber, etc.) and different grid resolutions. The results for the wind tunnel with no diffuser section (Figure 2) are discussed in the following sections. Viscous boundary conditions were used for the tunnel walls in FUN3D simulations.

Roe's approximate Riemann solver [22] was used for the inviscid flux with no flux limiting in all simulations. The Spalart-Allmaras turbulence model [23] with the rotation-curvature correction [24], and the quadratic constitutive relation [25] was used for turbulence calculations. In the wind tunnel test, the flow was tripped at x = 336 mm from the nose as well as on the upper and lower wing surfaces, whereas, all CFD simulations were run in the fully turbulent mode.

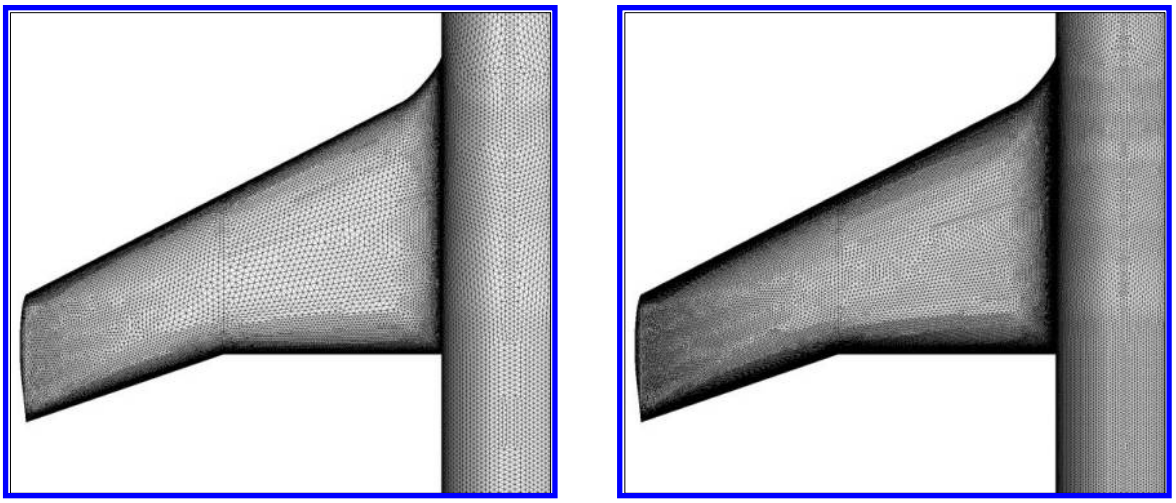

Figure 1. A zoomed view of the Juncture Flow Model coarse mesh (~11 million nodes) and the medium mesh (~36 million nodes) used in the current study.

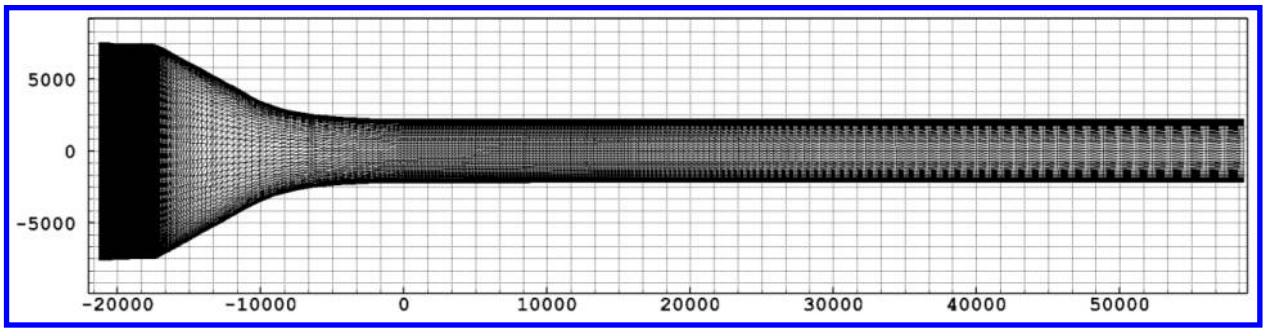

Figure 2. 14x22 Subsonic Tunnel grid without the diffuser section (~8 million nodes). Units are in millimeters.

In order to generate the coarse and medium resolution overset grids, the free-air grids were first reflected across the symmetry plane to obtain grids for full-span JF models with approximately 21 million and 71 million nodes for the coarse and medium resolutions, respectively. The free-air full-span JF grid was rotated by the angle of attack, and integrated with the 14x22 grid to obtain the overset grid using SUGGAR++ [26]. The final coarse and medium overset grids had approximately 29 million and 79 million nodes, respectively. The free-air and in-tunnel grid sizes are compared in Table 2. SUGGAR++ generates the grid connectivity information along with the final composite grid, which is used by FUN3D for interpolation between the two component grids. In the FUN3D simulations, the overset grids were rotated by the angle of attack – this was done in order to avoid coordinate transformation of measurements for comparison. Figure 3 shows the final overset assembly used in the simulation for the 5° angle of attack case. The mast and sting used to mount the juncture flow model in the wind tunnel test have not been taken into account in these simulations.

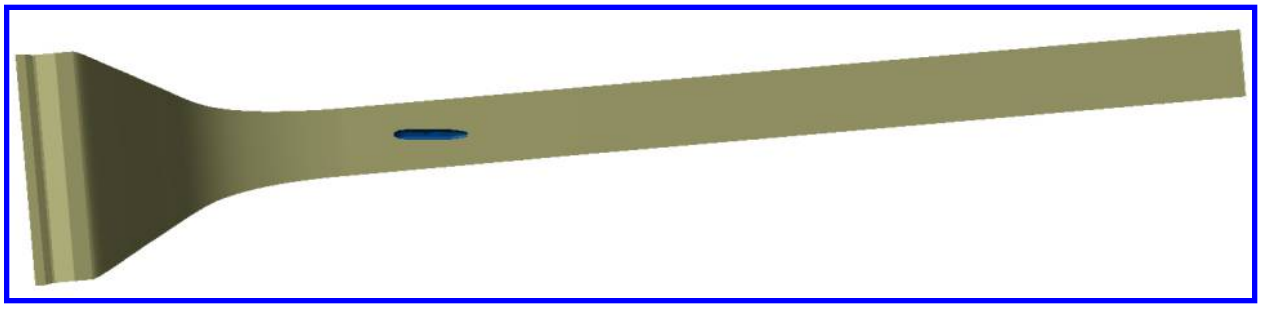

Figure 3. The JF model in 14x22 composite grid generated using SUGGAR++. The coarse and medium overset grids had approximately 29 million and 79 million nodes, respectively.

Since the viscous loss at the outflow boundary is not known a priori, the static pressure at the outflow is usually iterated manually to match the tunnel conditions [14] in the wind tunnel simulations. Carlson has automated this procedure in FUN3D using a proportional-integral-derivative (PID) controller [17]. Total pressure measured near the start of the contraction section and the static pressure measured near the start of the test section are used in the tunnel calibration equations to adjust the back pressure while maintaining the desired tunnel conditions with the help of the PID controller. The tunnel conditions in the simulation can be set either in terms of the Reynolds number or the Mach number. In the present simulations, a target Reynolds number equal to the reference Reynolds number was specified. The PID controller was invoked every one thousand iterations to adjust the back pressure boundary condition in order to maintain the target Reynolds number.

Table 2: Grid Size (Number of Nodes).

Grid	Free-air	In-tunnel
Coarse	10.7 million	29.3 million
Medium	35.7 million	79.2 million

A typical in-tunnel simulation can take 120,000 iterations to converge (a reduction of 5–6 orders of magnitude in residuals). Figure 4 shows a typical time history of the residuals (mean quantities and turbulence) and the PID controller data. At around 110,000 iterations, the Reynolds number and the Mach number have almost approached the tunnel conditions based on the target Reynolds number. The peaks in the residuals time history correspond to calls to the PID controller routine. Although not shown, the convergence and PID controller time histories for –2.5° and 7.5° angles of attack cases show similar trends.

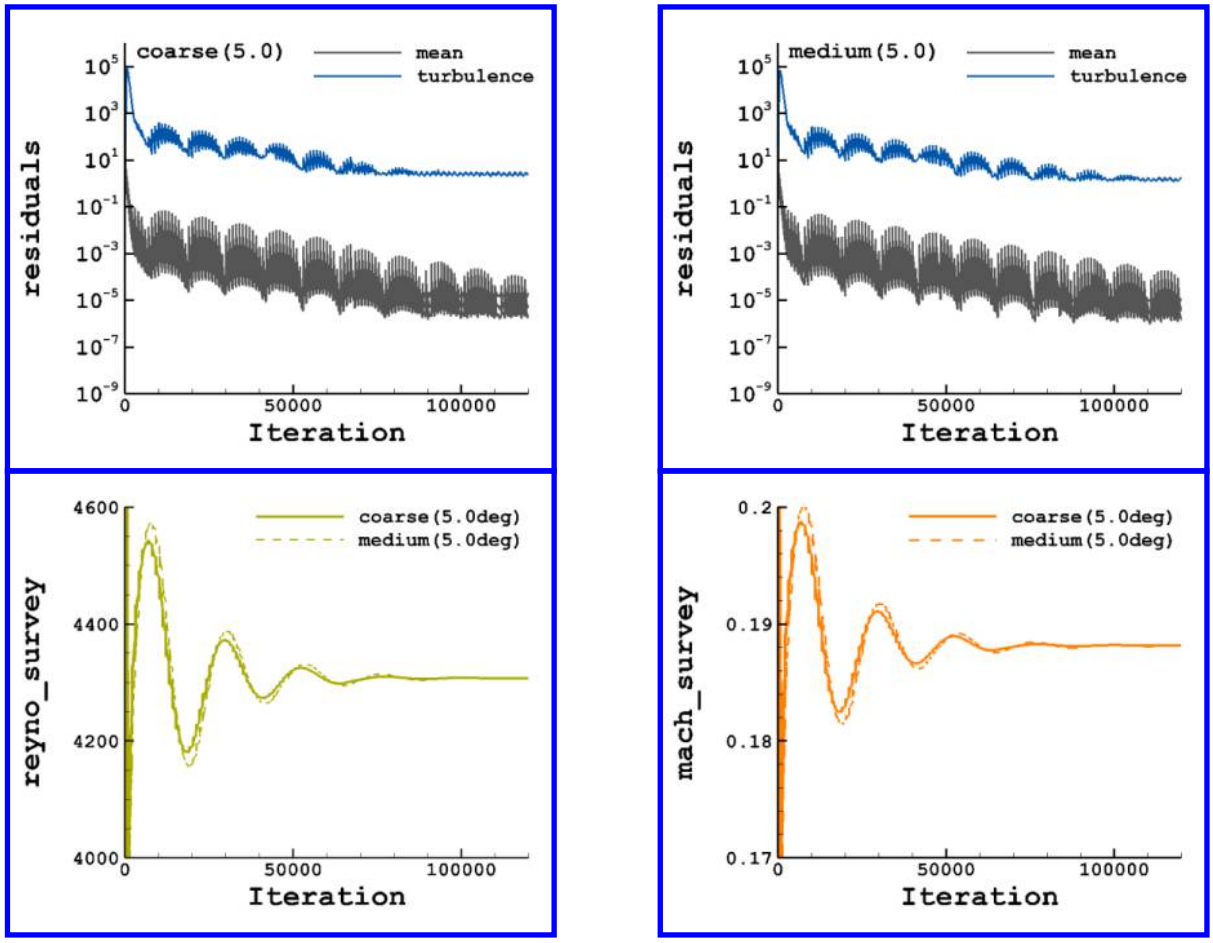

Figure 4. Convergence and PID tunnel controller time history: $\alpha = 5°$.

B. Separation Size

The prediction of separation initiation location (x coordinate of the separation point) along with the difference in the computed and measured values is listed in Tables 3–5 for reference. To estimate the separation initiation location, the slice on the wing-fuselage juncture at y = –236.1 mm was extracted and the x coordinate of the separation point was defined as the location where the x component of the skin friction ($C_{f,x}$) was zero. Figure 5 shows the comparison of $C_{f,x}$ predicted by the free-air and the in-tunnel simulations on the medium grids for α = 5° and α = 7.5° cases. The free-air predictions of the bubble length are closer to the measurements in all cases, but the differences are very small. In general, all CFD runs using the SA-RC-QCR2000 turbulence model predict early separation (overestimate the separation bubble length) compared with experiment.

Comparison of the flow separation prediction in the juncture region using free-air and in-tunnel grids is shown in Figures 6–8 for the three angles of attack. The results of the simulations in terms of both shape and size are qualitatively similar for the –2.5°, 5.0°, and 7.5° angles of attack. In general, the differences in separation bubble sizes due to grid resolution are larger than compared to whether the simulation was run as free-air or in-tunnel. Lee and Pulliam [14] have also reported small differences in both the bubble shape and size between the free-air and in-tunnels runs on medium and fine resolution grids using OVERFLOW. The change in the bubble width due to increased mesh resolution is more pronounced compared to the bubble length, and the tunnel walls again have very little effect.

Table 3: Separation Initiation Location (Measured x = 2893 ± 9.6 mm) α = –2.5°.

Run	Coarse (mm)	Difference (mm)	Medium (mm)	Difference (mm)
Free-air	2822.9	70.1	2840.0	53.0
In-Tunnel	2821.0	72.0	2837.5	55.5

Table 4: Separation Initiation Location (Measured x = 2851 ± 15.1 mm) α = 5°.

Run	Coarse (mm)	Difference (mm)	Medium (mm)	Difference (mm)
Free-air	2753.8	97.2	2784.9	66.1
In-Tunnel	2749.9	101.1	2781.1	69.9

Table 5: Separation Initiation Location (Measured x = 2837 ± 17.1 mm) α = 7.5°.

Run	Coarse (mm)	Difference (mm)	Medium (mm)	Difference (mm)
Free-air	2738.8	98.2	2771.9	65.1
In-Tunnel	2735.4	101.6	2767.6	69.4

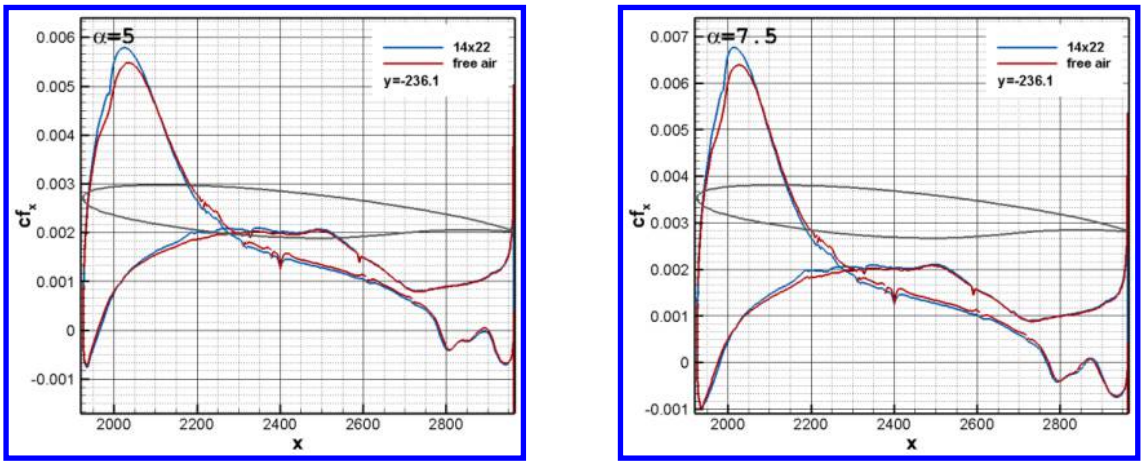

Figure 5. $C_{f,x}$ slice at y = –236.1 mm, α = 5° (left) and α = 7.5° (right).

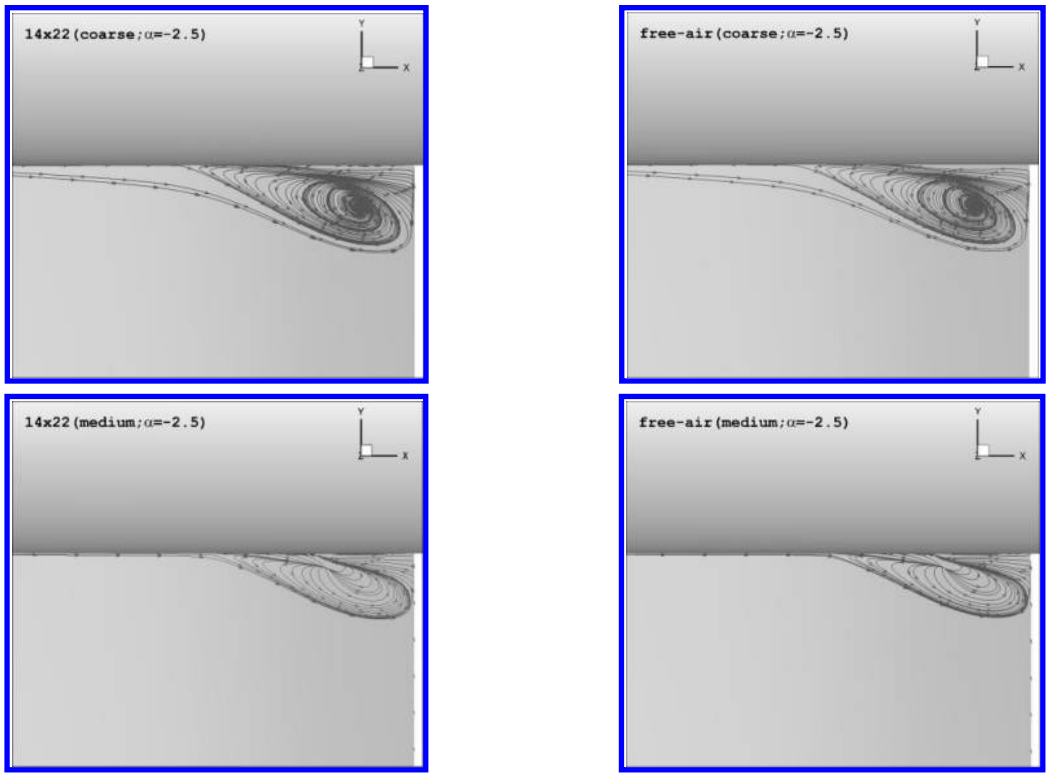

Figure 6. Flow separation in the wing-fuselage juncture region on the coarse and medium resolution in-tunnel and free-air grids, α = –2.5°. The flow direction is from left to right.

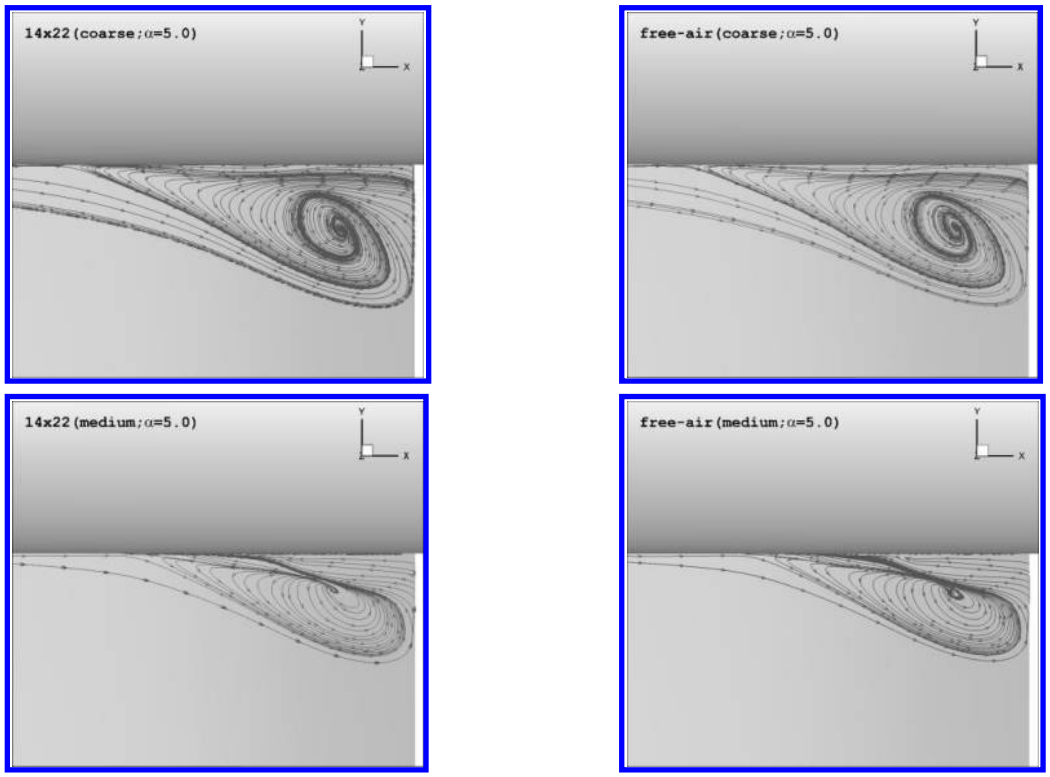

Figure 7. Flow separation in the wing-fuselage juncture region on the coarse and medium resolution in-tunnel and free-air grids, α = 5°. The flow direction is from left to right.

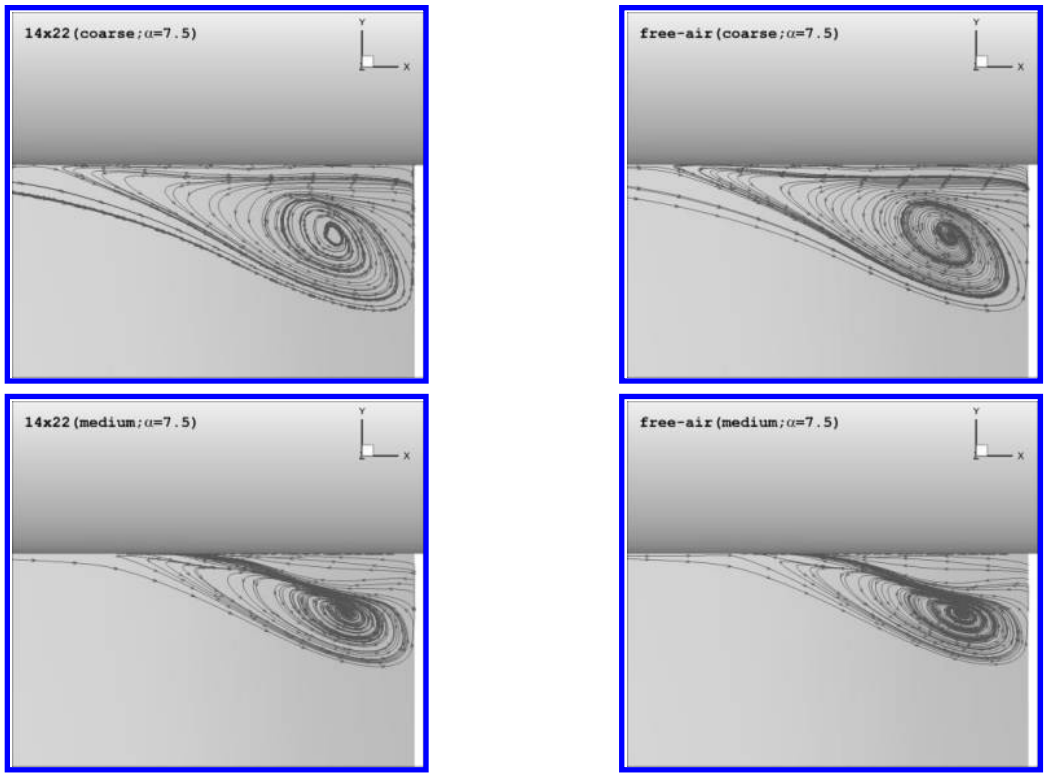

Figure 8. Flow separation in the wing-fuselage juncture region on the coarse and medium resolution in-tunnel and free-air grids, α = 7.5°. The flow direction is from left to right.

C. Surface Pressures

Figures 9–10 show the comparison of the measured and computed surface pressure coefficients for α = –2.5°, 5°, and 7.5° on the wing for the medium mesh. In the latest phase of the JF experiment, measurement uncertainty in the pressure coefficients was estimated from the multiple data collection runs in which data were obtained on both the port and starboard wings. The uncertainty in the surface pressure measurements shown in the plots is quite small. Overall, the computed surface pressure values on the wing compare well with the measurements, and the differences between the in-tunnel and free-air results are relatively small for all angles of attack.

In the case of α = 5° and α = 7.5°, the in-tunnel peak C_p prediction on the upper surface of the wing is closer to the measurements compared to the free-air runs. Similar differences were also observed in the comparison of in-tunnel vs. free-air simulations using OVERFLOW [14] and FUN3D [15]. The peak in C_p at the leading edge of the inboard station (y = –254 mm) is underestimated in the free-air simulations and is captured better by the in-tunnel simulations. The C_p prediction at the trailing edge near the wing-fuselage juncture (y = –254 mm) is off in both the in-tunnel and free-air simulations. Previous studies using different codes have also reported this discrepancy. Rumsey et al. have shown a significant improvement in the separation size and surface pressure predictions at this location with their improved QCR2020 turbulence scheme [27].

The in-tunnel simulations overestimate the surface pressure peak near the leading edge at the outboard stations on the wing (y = –685.8 mm, –994.92 mm, and –1295.4 mm). The differences between the in-tunnel and free-air predictions are pronounced at y = –1663.7 mm near the wing tip. The surface pressure predictions also show a marked improvement with increased grid resolution at this station (not shown in the figures).

Figure 11 shows the comparison of the measured and computed surface pressure coefficients for α = –2.5°, 5°, and 7.5° on the fuselage. Both the free-air and in-tunnel simulation results are in reasonable agreement with the measurements for all angles of attack. The free-air C_p prediction on the fuselage is slightly closer to the measurements compared to the in-tunnel runs.

In general, the in-tunnel simulations show small improvements in the C_p prediction when compared with free-air simulations at certain stations on the wing. However, these differences are smaller when compared to differences observed at different mesh resolutions or by using different turbulence schemes [8, 12–15].

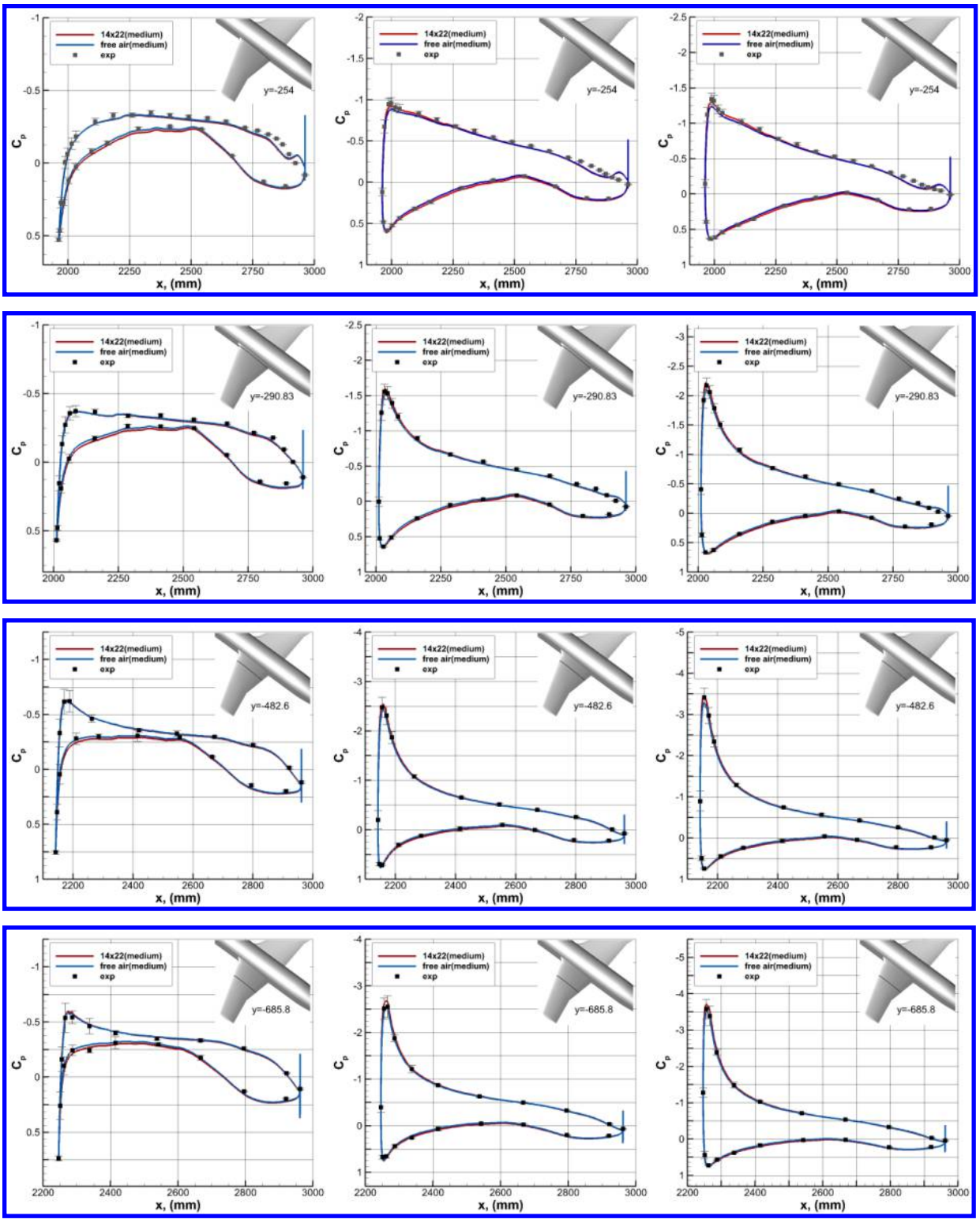

Figure 9. Pressure coefficients on the wing, α = –2.5° (left), α = 5° (center), α = 7.5° (right).

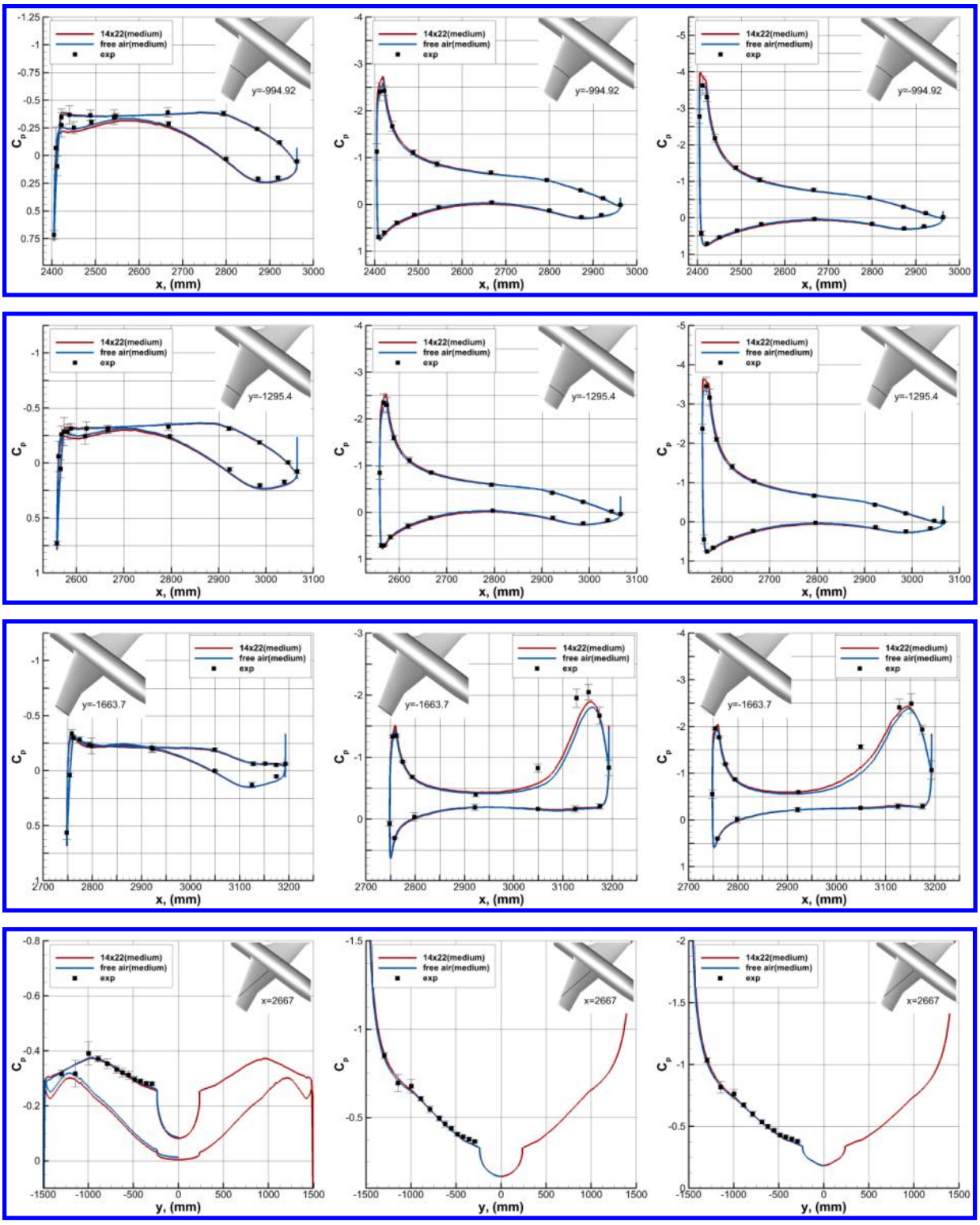

Figure 10. Pressure coefficients on the wing, α = –2.5° (left), α = 5° (center), α = 7.5° (right).

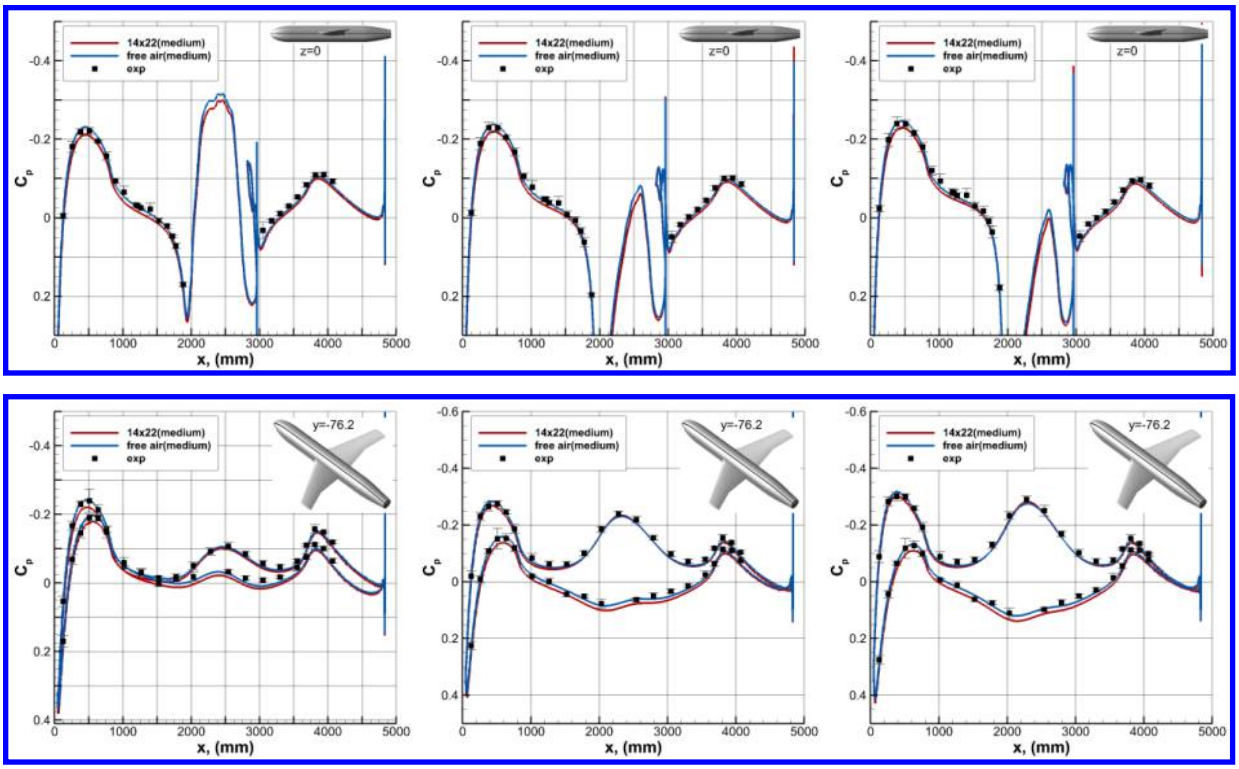

Figure 11. Pressure coefficients on the fuselage, α = –2.5° (left), α = 5° (center), α = 7.5° (right).

D. Comparison with LDV data

The in-tunnel and the free-air simulation data for α = –2.5° and 5° cases are compared with the LDV profiles in Figure 12 at a point near the nose on the fuselage at x = 1168.4 mm, z = 0. LDV data for α = 7.5° were not taken at this location. Overall, the mean velocities are in reasonable agreement with the data on the fuselage with some discrepancy in the prediction of the u component profile. With the exception of two components of the normal stresses ($u'u'$ and $w'w'$), the rest of the turbulence quantities also match the measurements fairly well. The differences between the in-tunnel and free-air simulations and due to increased mesh resolution are not noticeable at this location.

In the latest JF experiment, LDV data were also collected for α = 7.5°. In addition to the point profiles, planes of data were collected at selected locations. Figures 13–21 show the comparison of the LDV data collected in the y-z plane at x = 2747.6 mm with the simulation data for all three angles of attack. This plane is upstream of the separation location on the wing. The free-air and in-tunnel data on the medium grid are shown in the plots. A qualitative comparison of the simulation data with measurements shows reasonable agreement in the mean component of velocities at all angles of attack. This agreement is in terms of both the magnitude and the spatial topology of the flow field. The $u'u'$ and $v'v'$ components of the normal stress are underestimated, and the $w'w'$ component is overestimated near the walls by the model. There is also agreement in qualitative terms between the measurements and the models, in the shear stress components. The $u'w'$ and $v'w'$ components of the shear stress are overestimated by the models. Only relatively small differences can be observed between the in-tunnel and the free-air predictions for all quantities at this location.

Figure 22 shows the comparison of the free-air and in-tunnel simulation results with the LDV data taken on the wing downstream of the separation. Results are shown for α = 5°, at (x, y) = (2852.6 mm, –266.1 mm) and, α = 7.5° at (x, y) = (2892.6 mm, –246.1 mm). At the locations selected on the wing for the two angles of attack, the CFD has already separated too far upstream compared to the experiment. Therefore, its velocities and Reynolds stresses do not agree well with experiment. The effect of both wind tunnel walls and grid resolution is discernable at these locations inside the separated flow region, with the latter being significantly larger.

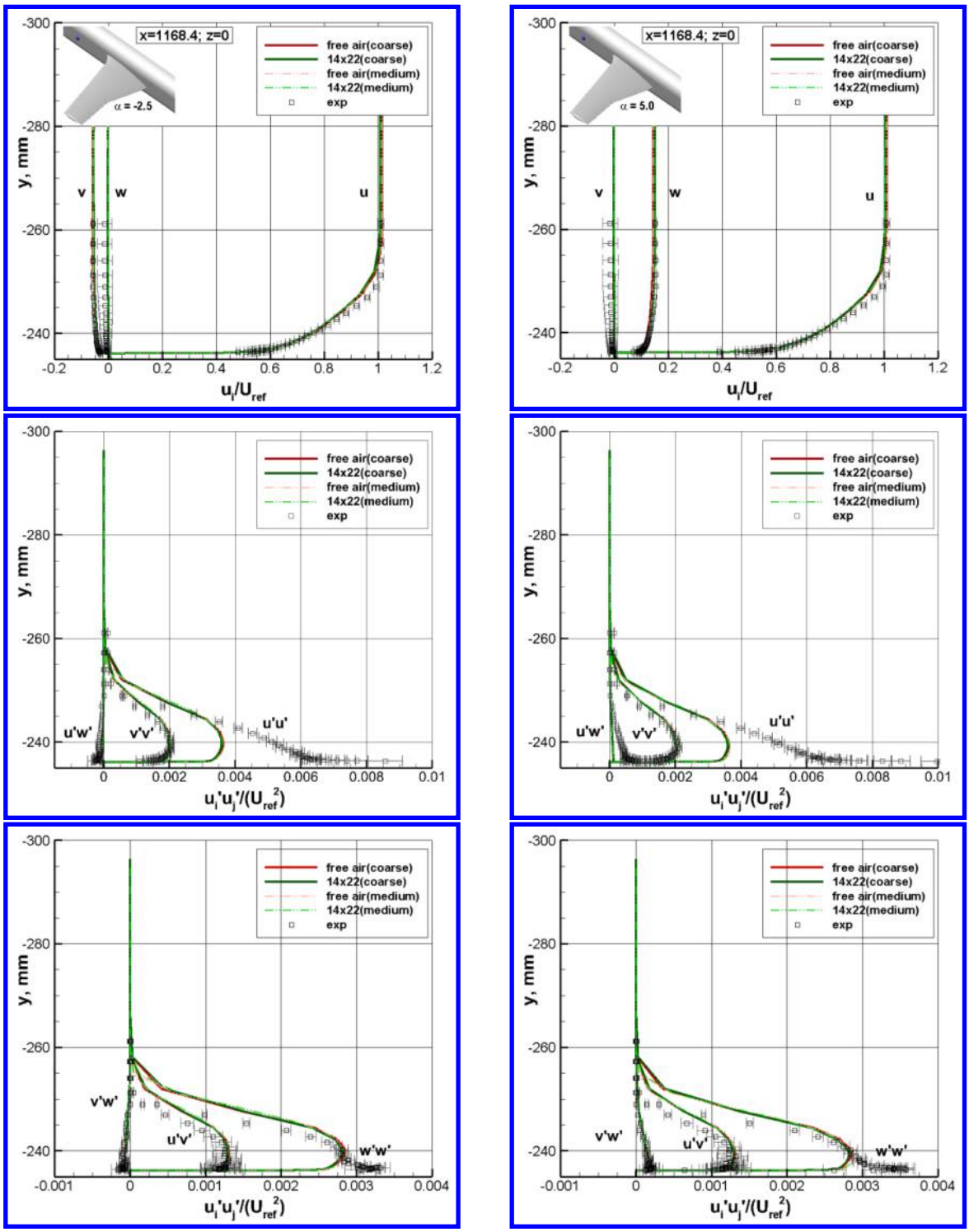

Figure 12. Comparison of the free-air and in-tunnel simulation results with the LDV data take on the fuselage, (*x*, *z*) = (1168.4 mm, 0). Coarse grid data are shown with solid lines and the medium grid data are shown with dash-dotted lines. Results are shown for α = –2.5°, and α = 5° in the left and the right columns, respectively.

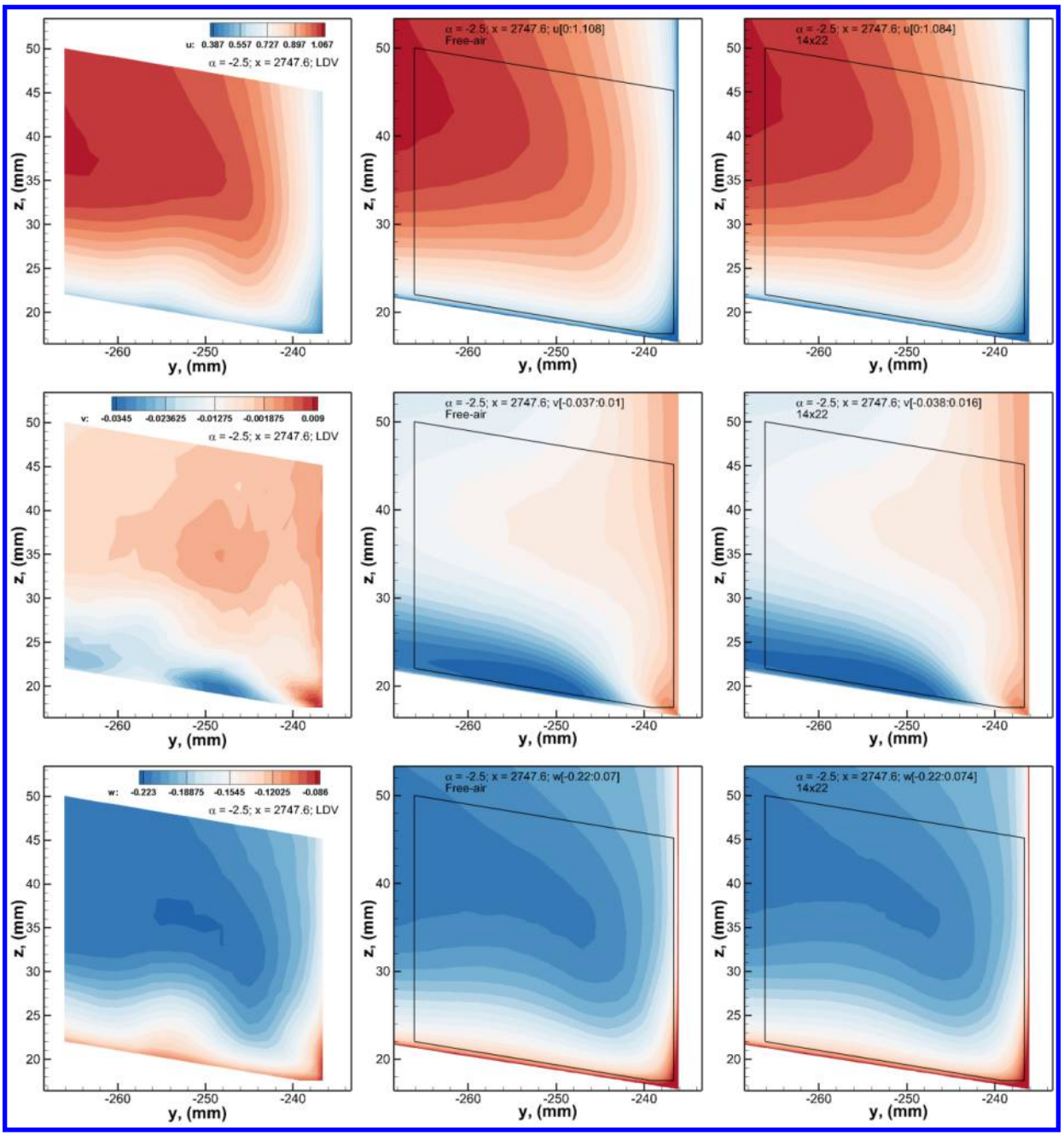

Figure 13. Comparison of the free-air and in-tunnel simulation results with the LDV data, α = –2.5°. LDV data (left), free-air (center), and in-tunnel simulation data (right). Simulation results are on the medium grid. Mean velocities in the wing-fuselage juncture are shown at *x* = 2747.6 mm. The black box in the simulation plots show the extent of the LDV data. The simulation plots are scaled by the LDV minimum and maximum.

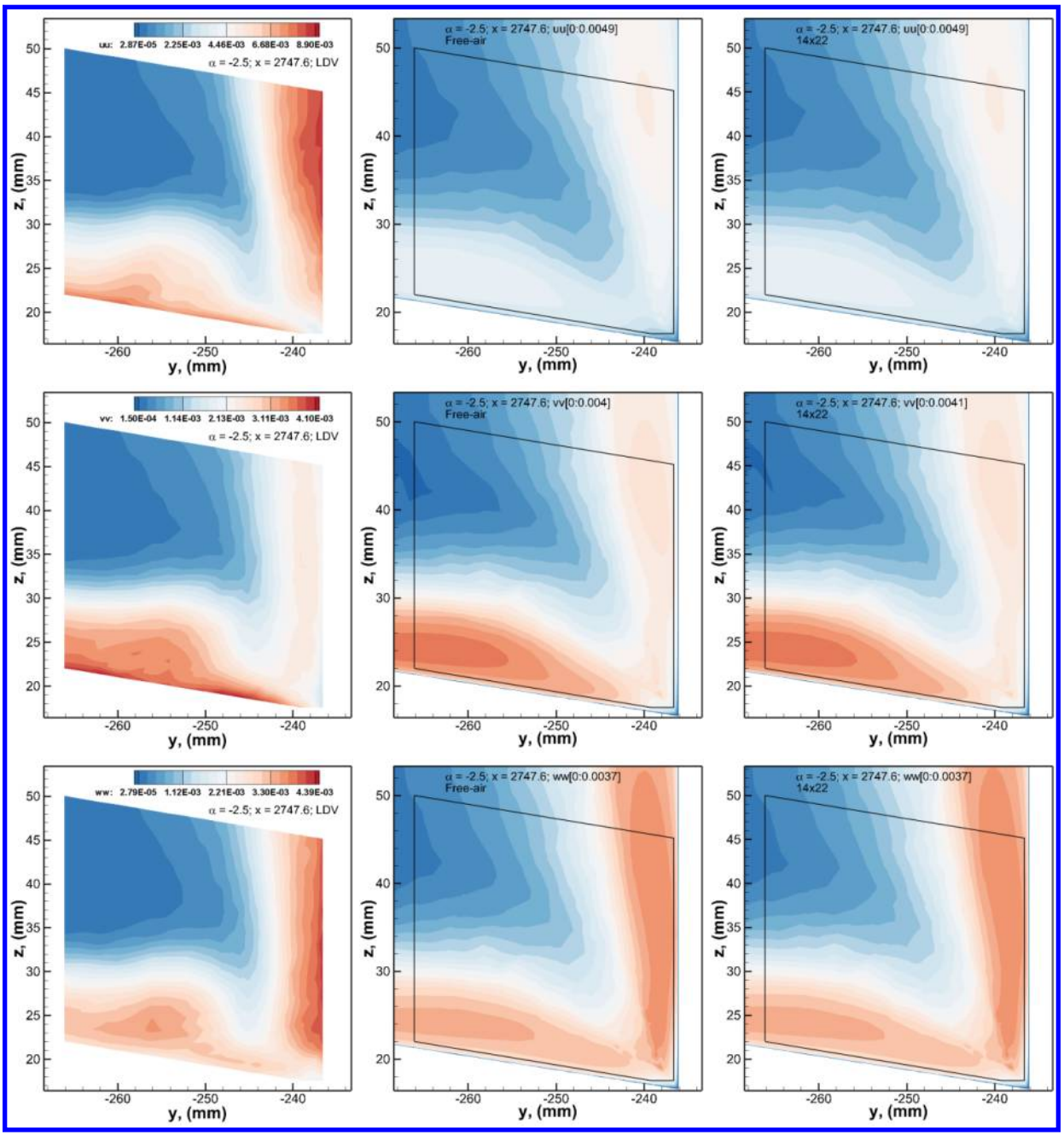

Figure 14. Comparison of the free-air and in-tunnel simulation results with the LDV data, α = –2.5°. LDV data (left), free-air (center), and in-tunnel simulation data (right). Simulation results are on the medium grid. Normal stresses in the wing-fuselage juncture are shown at *x* = 2747.6 mm. The black box in the simulation plots show the extent of the LDV data. The simulation plots are scaled by the LDV minimum and maximum.

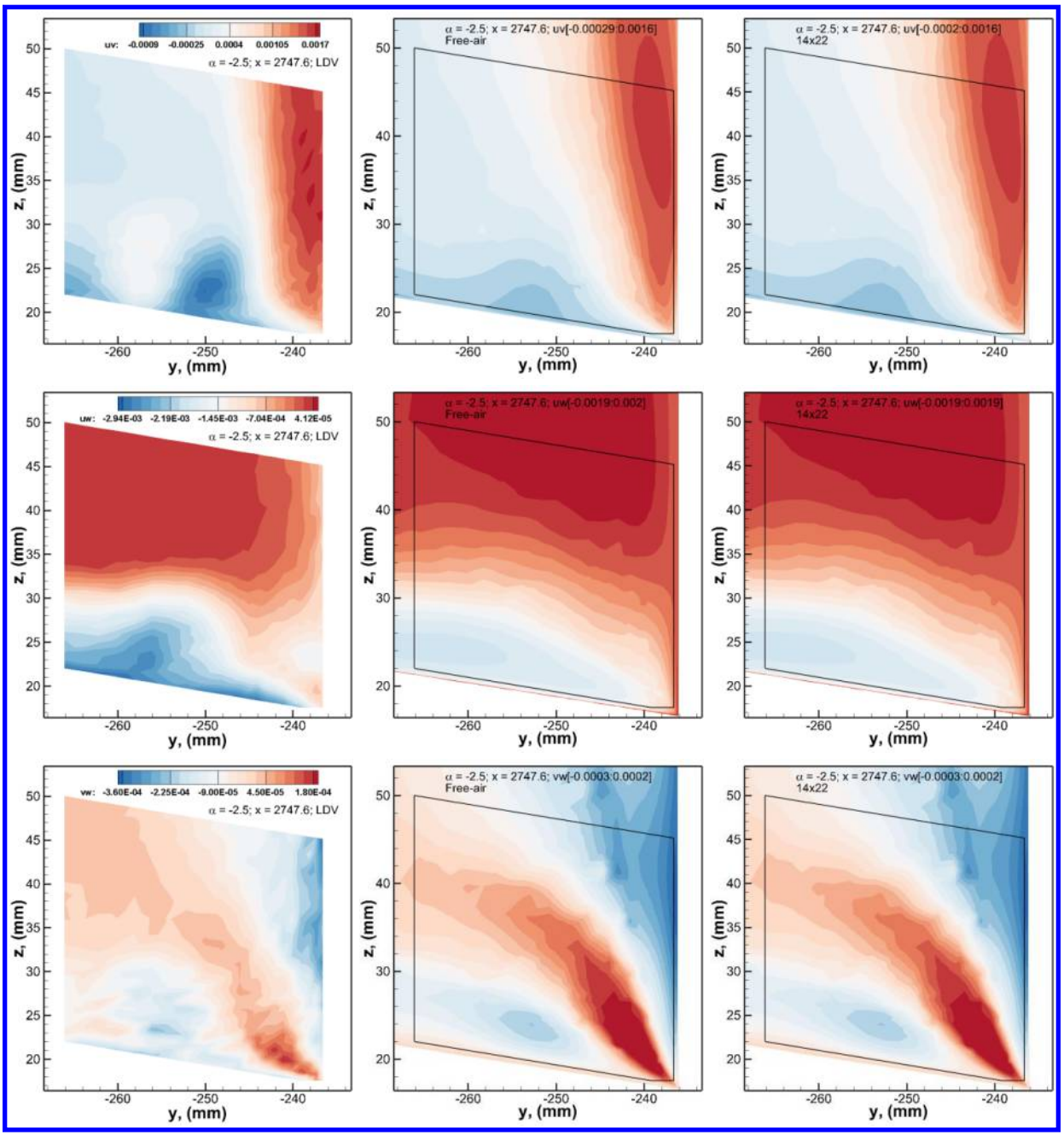

Figure 15. Comparison of the free-air and in-tunnel simulation results with the LDV data, α = –2.5°. LDV data (left), free-air (center), and in-tunnel simulation data (right). Simulation results are on the medium grid. Shear stresses in the wing-fuselage juncture are shown at *x* = 2747.6 mm. The black box in the simulation plots show the extent of the LDV data. The simulation plots are scaled by the LDV minimum and maximum.

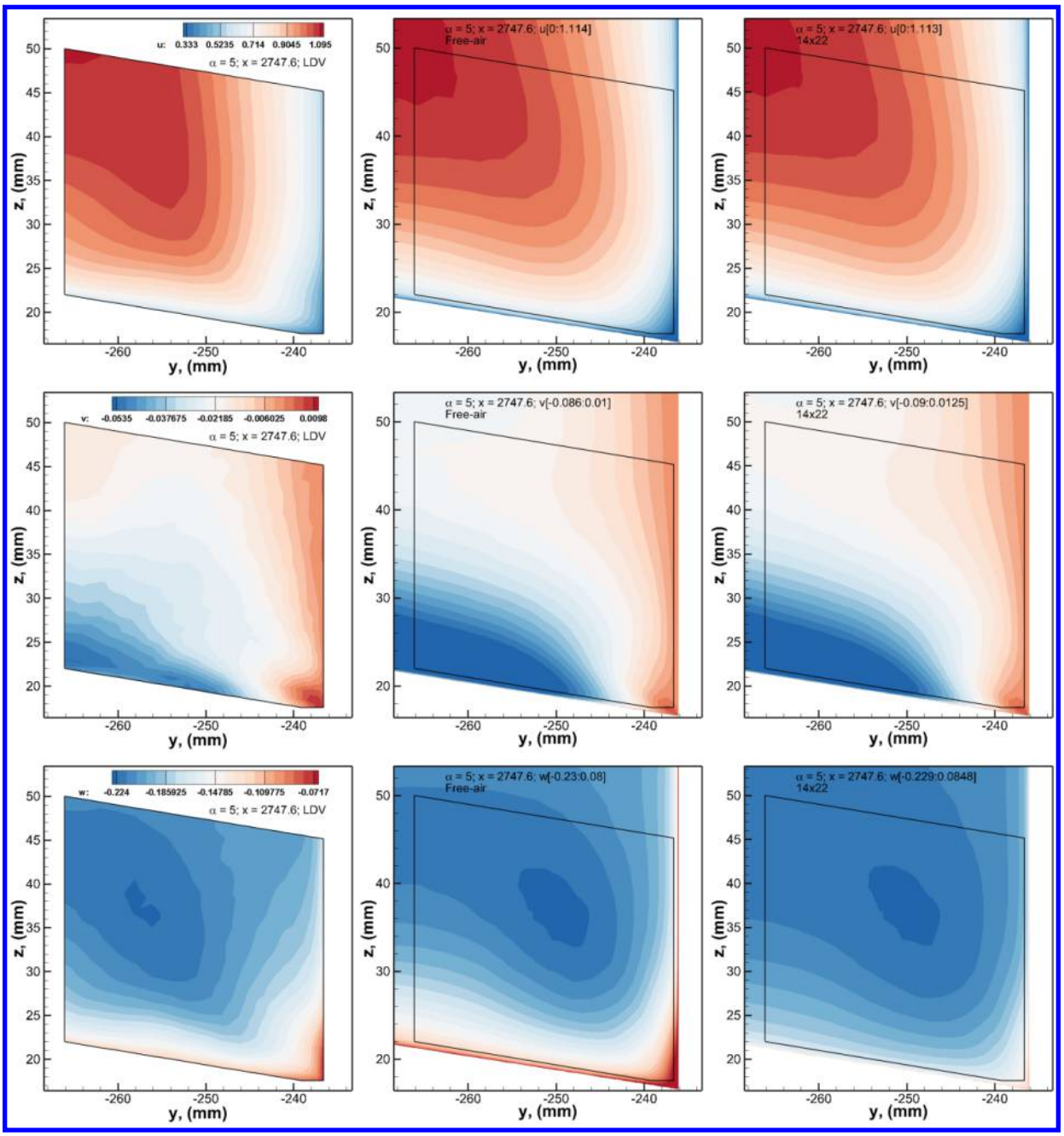

Figure 16. Comparison of the free-air and in-tunnel simulation results with the LDV data, α = 5°. LDV data (left), free-air (center), and in-tunnel simulation data (right). Simulation results are on the medium grid. Mean velocities in the wing-fuselage juncture are shown at *x* = 2747.6 mm. The black box in the simulation plots show the extent of the LDV data. The simulation plots are scaled by the LDV minimum and maximum.

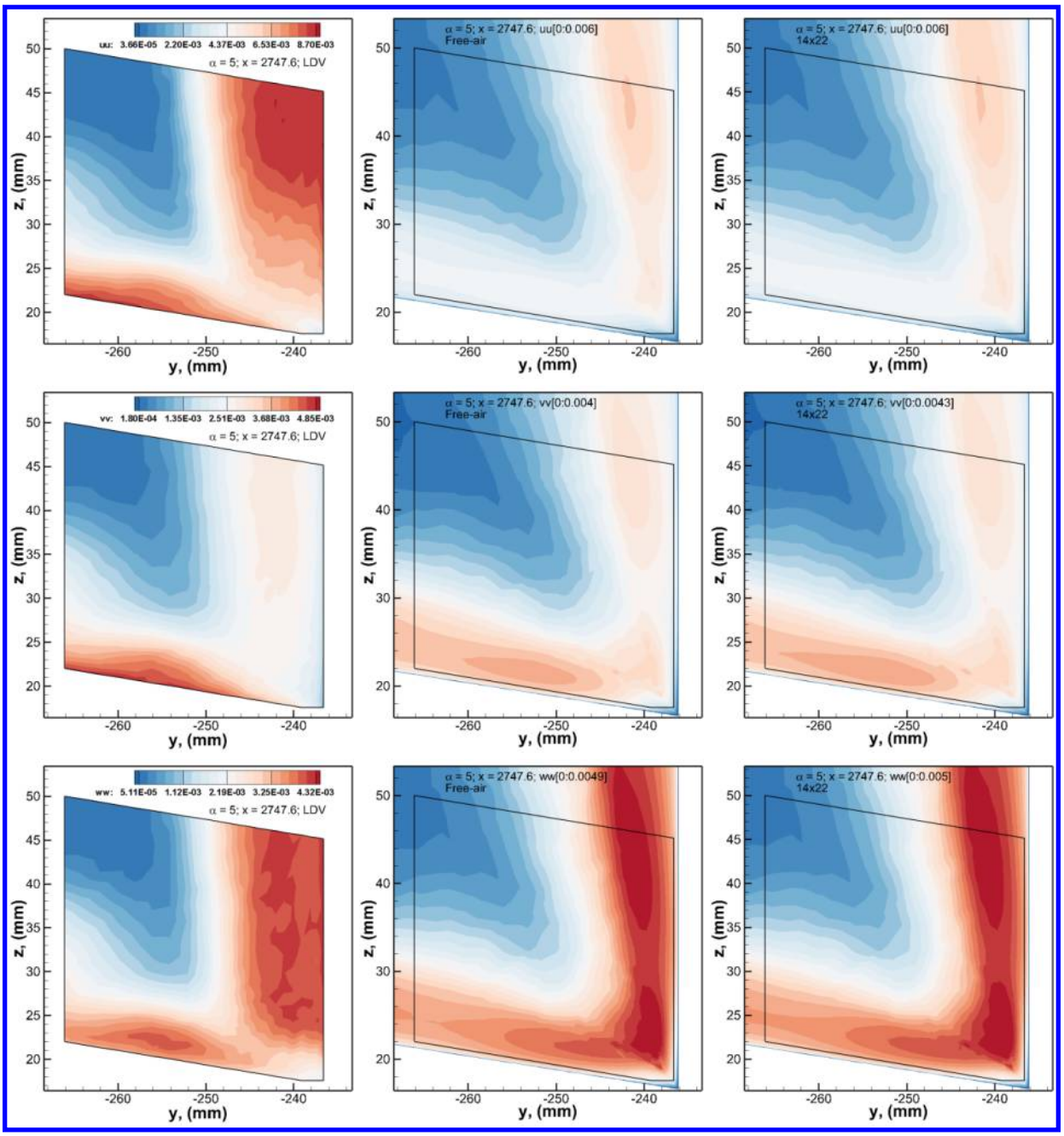

Figure 17. Comparison of the free-air and in-tunnel simulation results with the LDV data, α = 5°. LDV data (left), free-air (center), and in-tunnel simulation data (right). Simulation results are on the medium grid. Normal stresses in the wing-fuselage juncture are shown at *x* = 2747.6 mm. The black box in the simulation plots show the extent of the LDV data. The simulation plots are scaled by the LDV minimum and maximum.

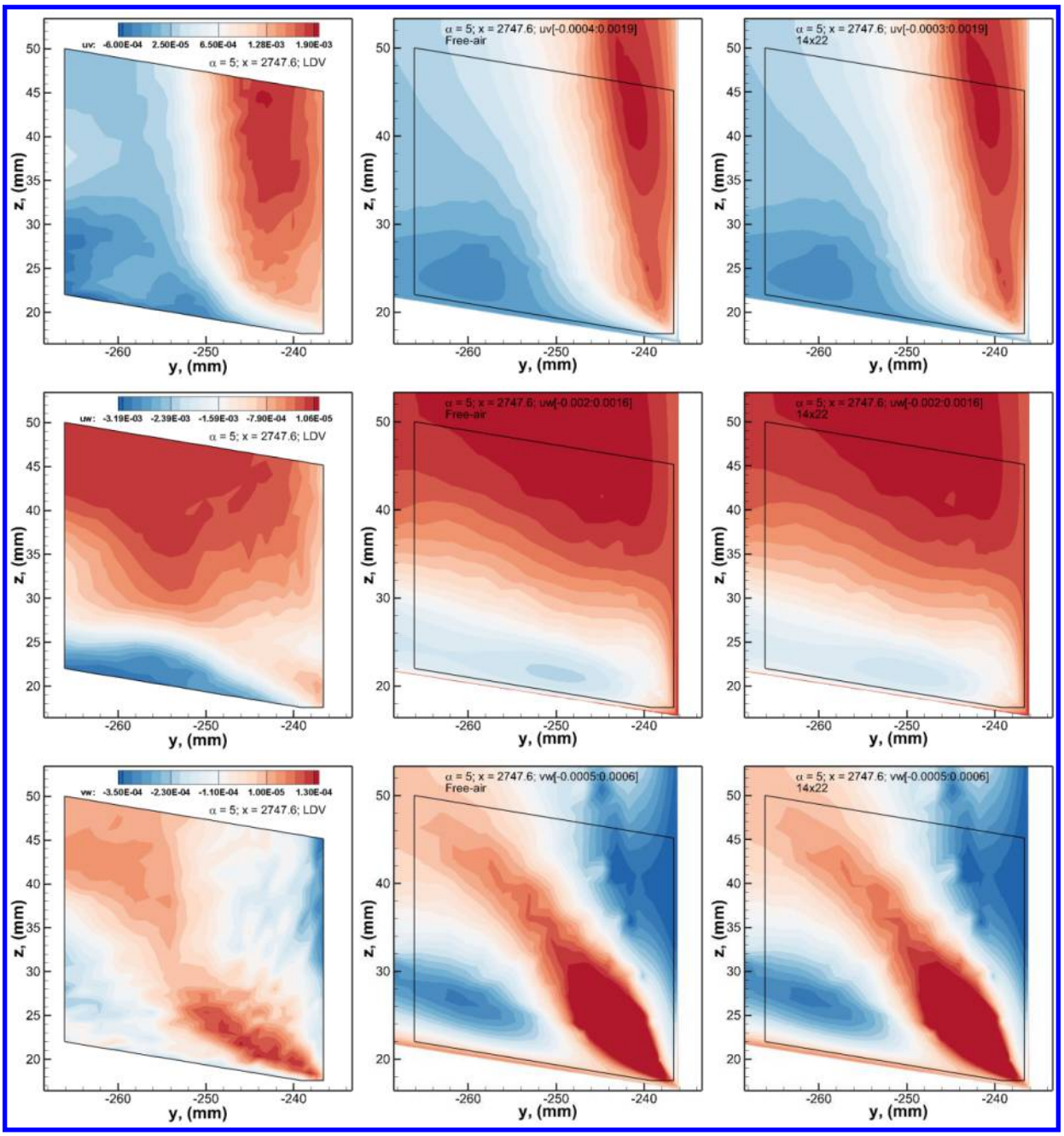

Figure 18. Comparison of the free-air and in-tunnel simulation results with the LDV data, α = 5°. LDV data (left), free-air (center), and in-tunnel simulation data (right). Simulation results are on the medium grid. Shear stresses in the wing-fuselage juncture are shown at *x* = 2747.6 mm. The black box in the simulation plots show the extent of the LDV data. The simulation plots are scaled by the LDV minimum and maximum.

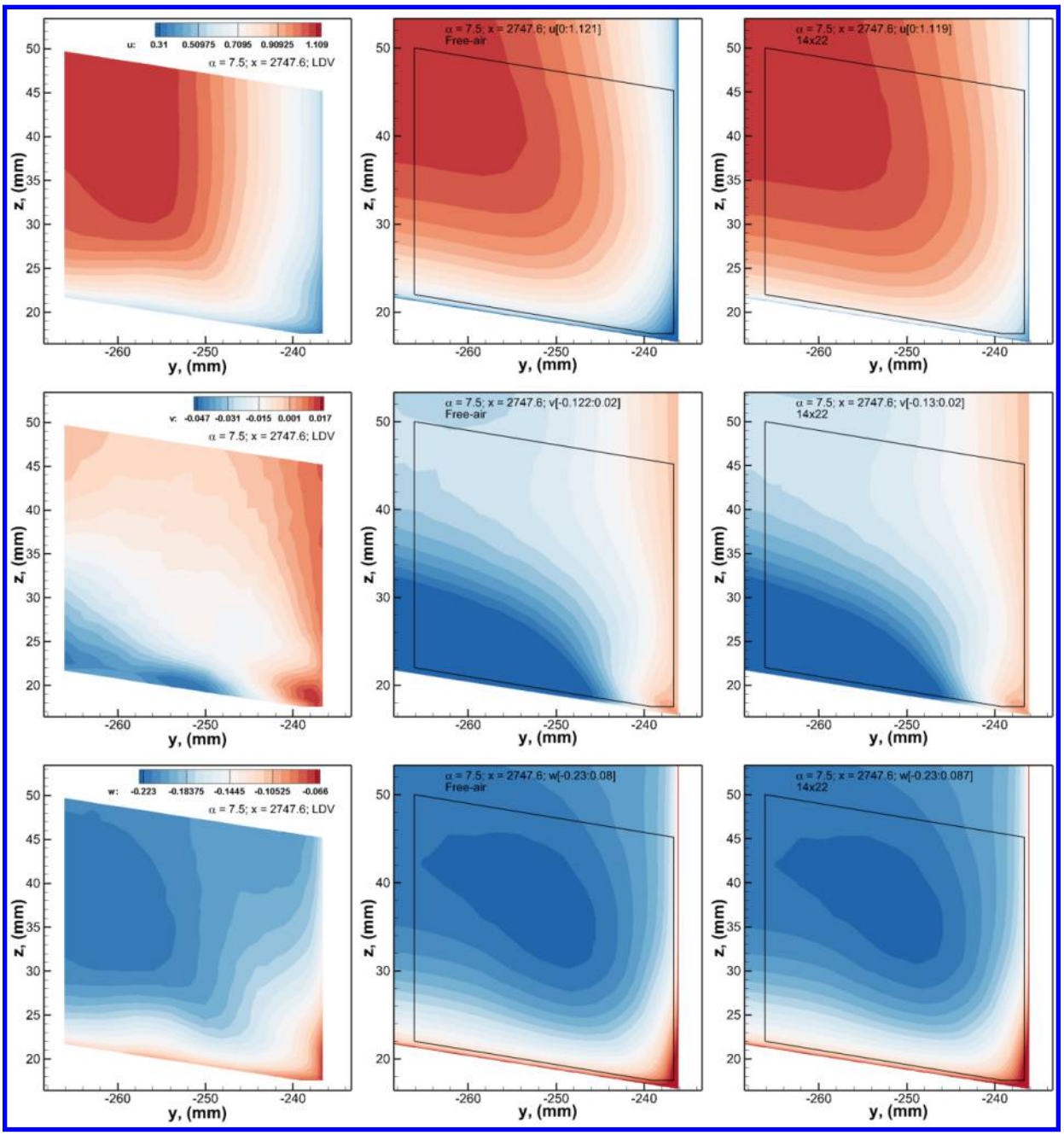

Figure 19. Comparison of the free-air and in-tunnel simulation results with the LDV data, α = 7.5°. LDV data (left), free-air (center), and in-tunnel simulation data (right). Simulation results are on the medium grid. Mean velocities in the wing-fuselage juncture are shown at *x* = 2747.6 mm. The black box in the simulation plots show the extent of the LDV data. The simulation plots are scaled by the LDV minimum and maximum.

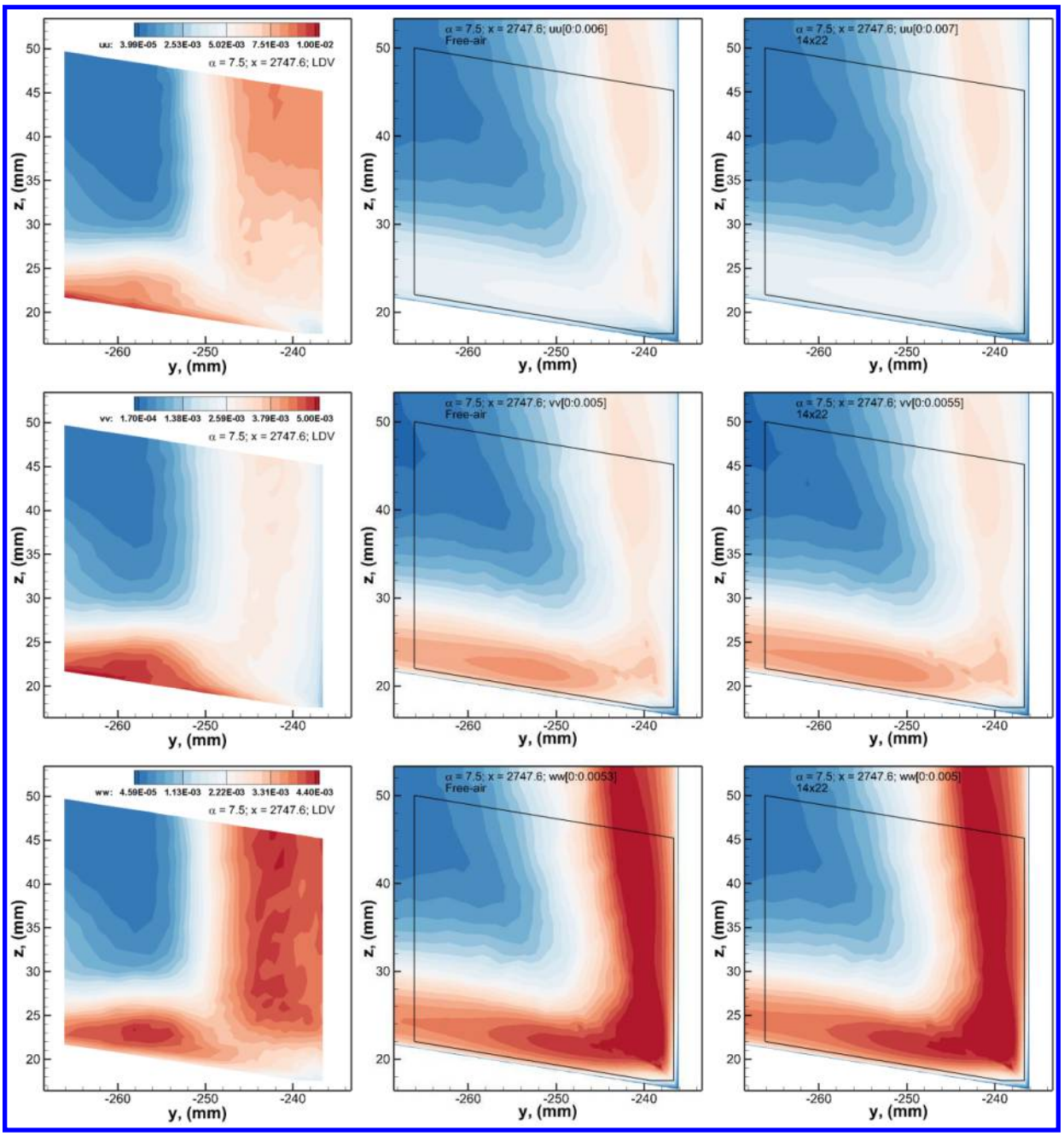

Figure 20. Comparison of the free-air and in-tunnel simulation results with the LDV data, α = 7.5°. LDV data (left), free-air (center), and in-tunnel simulation data (right). Simulation results are on the medium grid. Normal stresses in the wing-fuselage juncture are shown at *x* = 2747.6 mm. The black box in the simulation plots show the extent of the LDV data. The simulation plots are scaled by the LDV minimum and maximum.

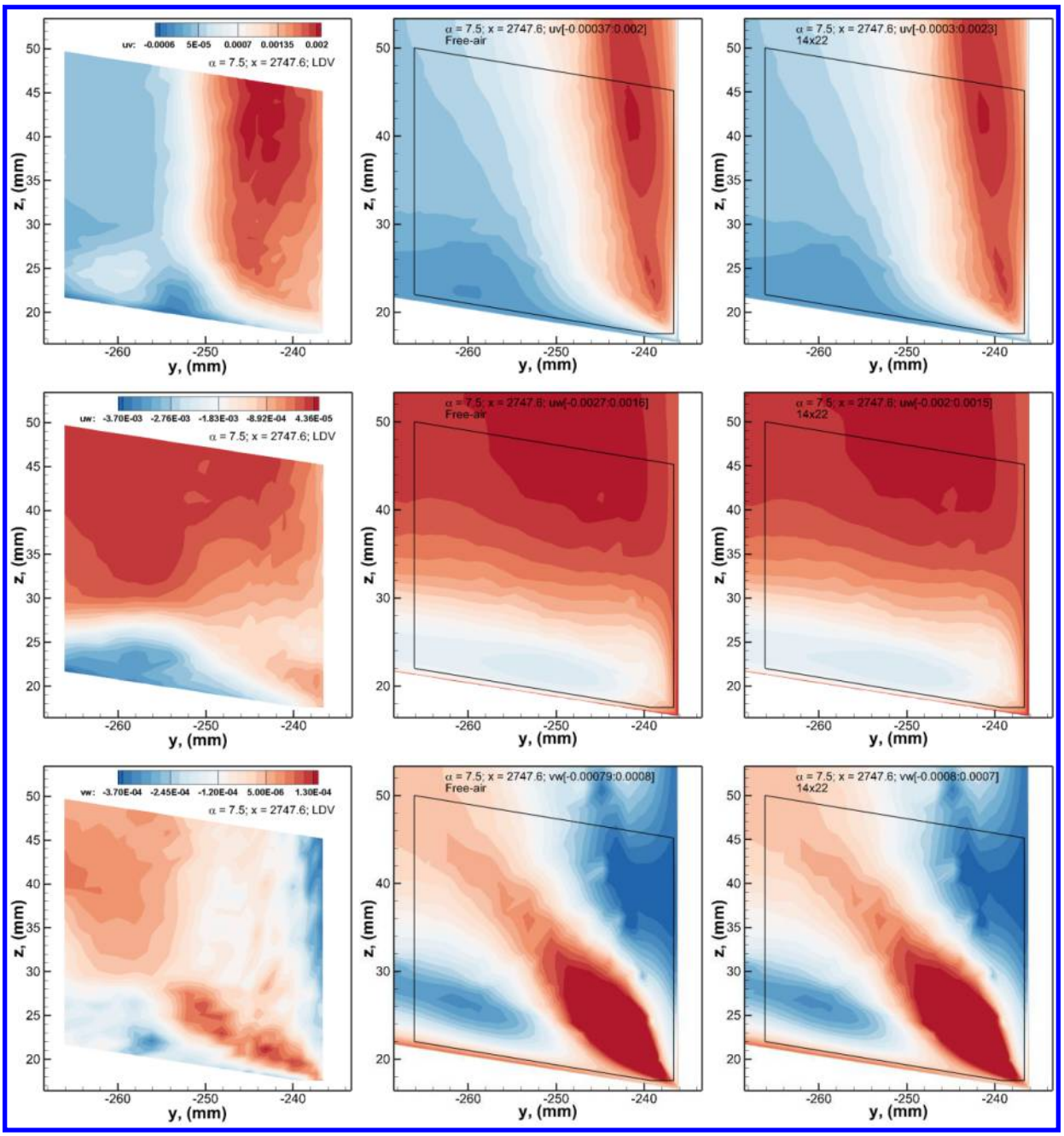

Figure 21. Comparison of the free-air and in-tunnel simulation results with the LDV data, α = 7.5°. LDV data (left), free-air (center), and in-tunnel simulation data (right). Simulation results are on the medium grid. Shear stresses in the wing-fuselage juncture are shown at *x* = 2747.6 mm. The black box in the simulation plots show the extent of the LDV data. The simulation plots are scaled by the LDV minimum and maximum.

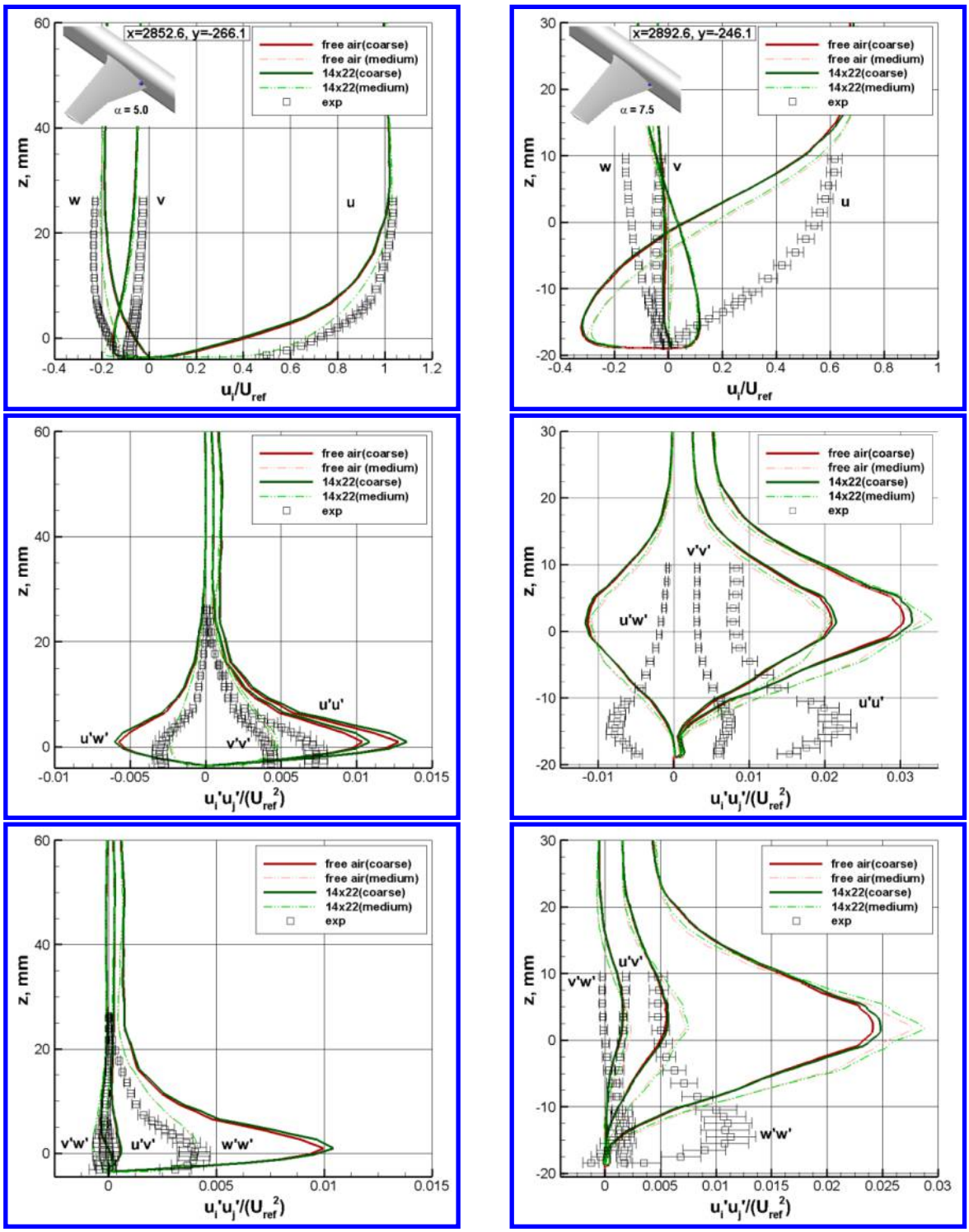

Figure 22. Comparison of the free-air and in-tunnel simulation results with the LDV data taken on the wing. Coarse grid data are shown with solid lines and the medium grid data are shown with dash-dotted lines. Results are shown for α = 5°, at (*x*, *y*) = (2852.6 mm, –266.1 mm) and, α = 7.5° at (*x*, *y*) = (2892.6 mm, –246.1 mm) in the left and the right columns, respectively.

IV. Sensitivity Runs

The in-tunnel simulations can take anywhere from 120,000 to 140,000 iterations to converge compared to 30,000 to 40,000 iterations for the free-air simulations. The convergence rate and behavior of the free-air simulations is much better than the in-tunnel simulations (10–11 orders of magnitude reduction in the residuals of the mean quantities compared to approximately 5–6 orders of magnitude reduction in the residuals for the in-tunnel simulations). Sensitivity runs were conducted in order to improve the convergence of in-tunnel simulations. These simulations included changing the frequency of the PID controller updates, and using Mach number as the target for the PID controller instead of Reynolds number, etc. The coarse mesh was used in these simulations for a quick turnaround and only the 5° angle of attack case was considered. Changing the frequency of the controller update had no effect on the convergence or the solution. However, specifying the Mach number as the target for the PID controller did improve the convergence behavior. A five order of magnitude reduction in residuals was achieved in 50,000 iterations when using the Mach number as the target compared to 90,000 iterations when using the Reynolds number as the target. Figure 23 compares the separation bubble in the wing-fuselage juncture for the two simulations. The bubble size and shape are almost identical for the two simulations. The x separation locations for the two runs were 2749.90 mm (target = Reynolds number) and 2749.86 mm (target = Mach number). Controller parameters at 120,000 iterations for the two simulations are given in Table 6. The Mach number at the tunnel survey location [17] is given in Table 6.

Table 6: Controller Parameters at 120,000 iterations into the Simulation, $\alpha = 5°$.

Target Parameter	Mach	P_{back}	$x_{separation}$
Reynolds Number	0.18814	0.99818	2749.90
Mach Number	0.18900	0.99794	2749.86

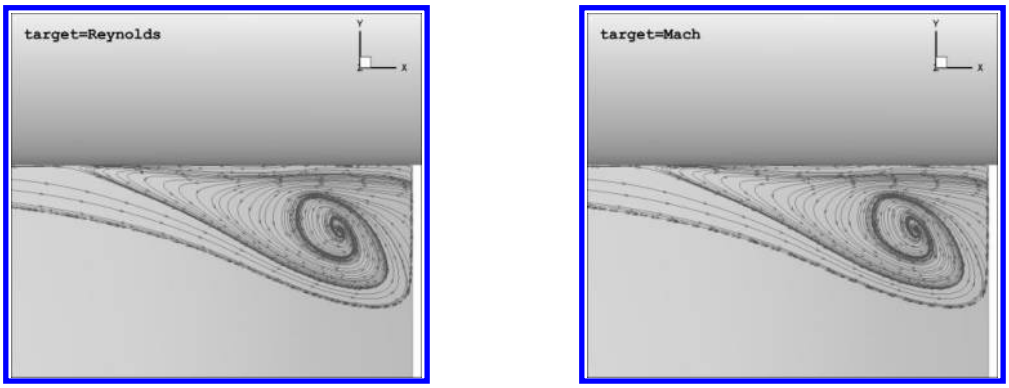

Figure 23. Effect of PID target on flow separation in the wing-fuselage juncture region, $\alpha = 5°$. The flow direction is from left to right.

The effect of including the wind tunnel diffuser section was also evaluated in this study. The mesh for the tunnel with diffuser (Figure 24) had approximately 10 million nodes and the corresponding coarse composite mesh resulted in 31.3 million nodes. An extended section of uniform cross section was added behind the diffuser section to minimize any adverse effects at the outflow boundary. This geometry (tunnel with the diffuser section) in the past has been difficult to simulate. Lee et al. [14] reported flow separation at the beginning of the diffuser section and the need for inviscid boundary conditions on the diffuser wall to avoid reverse flow.

In this study, all tunnel walls were specified as viscous boundaries. The FUN3D simulations could not be initialized using the second-order spatial reconstruction and required the first few thousand iterations (2000 iterations for the results shown here) to be first-order. Mach number was used as the PID controller target in these simulations and the rotation-curvature correction [24] was switched off. Figure 25 shows the pressure coefficients at selected locations on the wing and the fuselage for the two different tunnel geometries. A very slight improvement in C_p can be observed in the with-diffuser simulations but this difference is almost negligible. Figure 26 compares the separation bubble in the wing-fuselage juncture for the two simulations. The bubble size and shape are almost identical for the two simulations. The x separation locations for the two runs were 2737.20 mm (with diffuser) and 2737.15 mm (no diffuser).

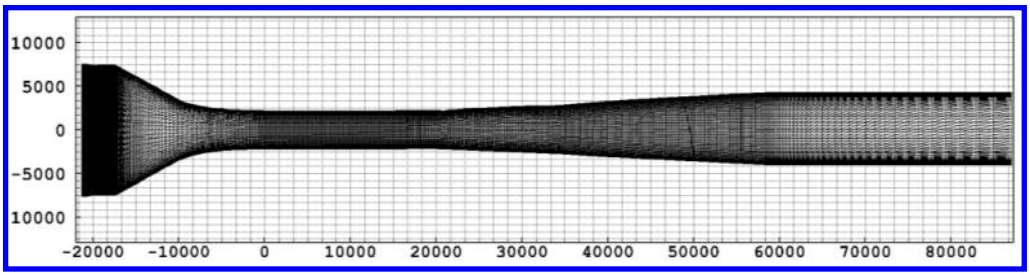

Figure 24. 14x22 Subsonic Tunnel Grid with the diffuser section (~10 million nodes). Units are in millimeters.

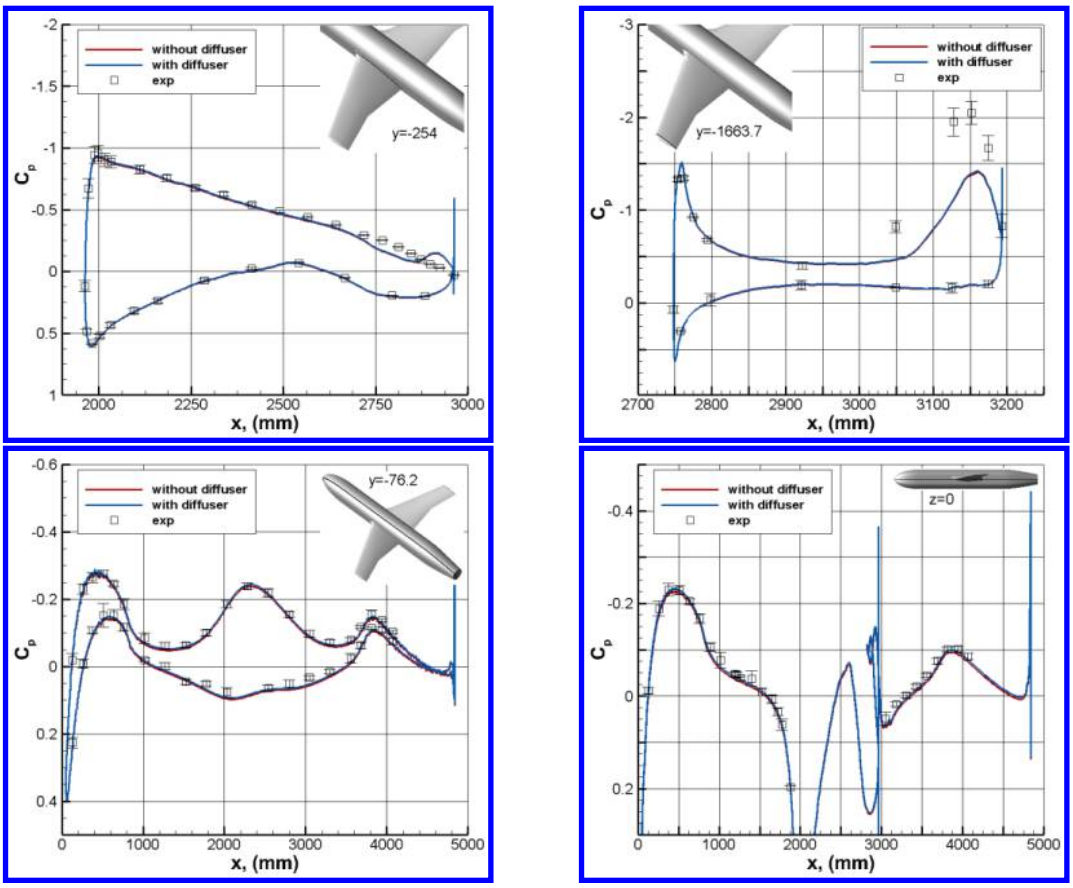

Figure 25. Pressure coefficients on the wing and the fuselage, α = 5°.

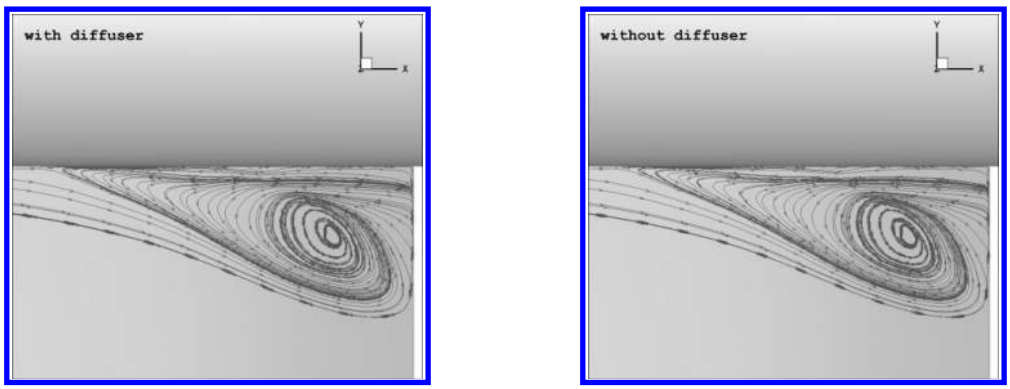

Figure 26. Flow separation in the wing-fuselage juncture region on the coarse grid, α = 5°. The flow direction is from left to right.

V. Summary

Free-air and in-tunnel simulations were compared with the Phase 2 Juncture Flow Experiment data for three angles of attack (α = –2.5°, 5°, and 7.5°). The surface pressure data on the wing and the fuselage compared well with the measurements. A slight underestimation in the pressure peak at the wing leading edge inboard station in the free-air simulations was alleviated in the in-tunnel simulation for α = 5° and α = 7.5° cases. The C_p prediction was also improved near the wingtip in the in-tunnel simulation for α = 5° and α = 7.5° cases. Differences between the in-tunnel and free-air surface pressures were negligible for the α = –2.5° case. The mean velocity profiles far upstream on the fuselage were predicted with a reasonably good degree of accuracy with small deviations in the *u* component of the mean velocity. With the exception of two components of the normal stresses ($u'u'$, $w'w'$), the rest of the turbulence quantities compared well with the measurements on the fuselage. This was observed for both α = –2.5° and α = 5°.

Comparison with the LDV data on the wing upstream of the separation showed good qualitative agreement with simulation data for all quantities and at all angles of attack. Relatively small differences were observed between the in-tunnel and the free-air predictions for all quantities at this location. Inside the juncture separation region large discrepancies in the mean velocities and turbulent stresses were observed compared with the LDV data, for both the free-air and in-tunnel simulations. The effect of mesh resolution was greater than differences between free-air and in-tunnel simulations at these locations.

No significant differences in the simulation results were observed when the diffuser section was added to the tunnel geometry. The bubble size and shape were almost identical for the two simulations. Differences observed between different mesh resolutions and between different turbulence schemes were larger than between free-air and in-tunnel simulations as well as in the comparison between simulations of tunnel with the diffuser section and the tunnel without the diffuser section.

In general, there were no significant differences in the prediction of the separation location, size, and shape, between the free-air and the in-tunnel runs. Only slight differences were observed in the bubble topology between the free-air and in-tunnel runs. As in previous simulations [13–15], the width of the bubble showed convergence toward the measured width size while the length was overestimated (A newer turbulence model variant [27], not used here, improves the predictions of separation). The differences in the bubble length at different mesh resolutions, and between the in-tunnel vs. free-air runs were not significant. The trends in all three angles of attack (–2.5°, 5° and 7.5°) were similar. The results of this study suggest that the effects of tunnel walls on the flow separation in the juncture region are relatively small.

Acknowledgments

This work was supported by the NASA TTT Project of the Transformative Aeronautics Concepts Program. The authors would like to thank the Juncture Flow Team members: Ponnampalam Balakumar, Judy Hannon, Luther Jenkins, Mike Kegerise, Cathy McGinley, Mujeeb Malik, Joe Morrison, and Dan Neuhart from NASA Langley; Henry Lee, Mike Olsen, and Tom Pulliam from NASA Ames; and Philippe Spalart from Boeing. Many thanks to Mike Wiese, Scott Brynildsen, and Norma Farr for providing the grids used in this study.

References

[1] Singh, D., König, B., Fares, E., Murayama, M., Ito, Y., Yokokawa, Y., Yamamoto, K., "Lattice-Boltzmann Simulations of the JAXA JSM High-Lift Configuration in a Wind Tunnel," AIAA Paper 2019–1333, doi: https://doi.org/10.2514/6.2019-1333.

[2] Ahmad, N.N., Proctor, F.H., Perry, B., "Numerical Simulation of the Aircraft Wake Vortex Flowfield," AIAA Paper 2013–2552, doi: https://doi.org/10.2514/6.2013-2552.

[3] Rumsey, C.L. and Morrison, J.H., "Goals and Status of the NASA Juncture Flow Experiment," NATO Science and Technology Organization, Specialists Meeting on Progress and Challenges in Validation Testing for Computational Fluid Dynamics, AVT–246–RSM–038, Avila, Spain, 26–28 September 2016, Paper Number AVT–246–03.

[4] Rumsey, C.L., Neuhart, D.H., Kegerise, M.A., "The NASA Juncture Flow Experiment: Goals, Progress, and Preliminary Testing (Invited)," AIAA Paper 2016–1557, doi: https://doi.org/10.2514/6.2016-1557.

[5] Rumsey, C.L., "The NASA Juncture Flow Test as a Model for Effective CFD/Experimental Collaboration," AIAA Paper 2018–3319, doi: https://doi.org/10.2514/6.2018-3319.

[6] Kegerise, M.A., Neuhart, D.H., "An Experimental Investigation of a Wing-Fuselage Junction Model in the NASA Langley 14– by 22–Foot Subsonic Wind Tunnel," National Aeronautics and Space Administration, NASA/TM–2019–220286, 2019.

[7] Levy, D.W., Laflin, K.R., Tinoco, E.N., Vassberg, J.C., Mani, M., Rider, B., Rumsey, C.L., Wahls, R.A., Morrison, J.H., Broderson, O.P., Crippa, S., Mavriplis, D.J., Murayama, M., "Summary of Data from the Fifth Computational Fluid Dynamics Drag Prediction Workshop," *Journal of Aircraft*, Vol. 51, 2014, pp. 1194–1212, doi: https://doi.org/10.2514/1.C032389.

[8] Rumsey, C.L., Ahmad, N.N., Carlson, J.-R., Kegerise, M.A., Neuhart, D.H., Hannon, J.A., Jenkins, L.N., Yao, C.-S., Balakumar, P., Bartram, S.M., Pulliam, T.H., Olsen, M.E., Spalart, P.R., "CFD Comparisons with Updated NASA Juncture Flow Data," AIAA SciTech Forum 2021.

[9] Rumsey, C.L., "NASA Langley Research Center Turbulence Modeling Resource," https://turbmodels.larc.nasa.gov, Accessed: 2020–11–01.

[10] NASA FUN3D CFD CODE, https://fun3d.larc.nasa.gov, Accessed: 2020–11–01.

[11] NASA OVERFLOW CFD CODE, https://overflow.larc.nasa.gov, Accessed: 2019–07–31.

[12] Rumsey, C.L., Carlson, J.-R., Ahmad, N.N., "FUN3D Juncture Flow Computations Compared with Experimental Data," AIAA Paper 2019–0079, doi: https://doi.org/10.2514/6.2019-0079.

[13] Rumsey, C.L., Lee, H.C., Pulliam, T.H., "Reynolds-Averaged Navier-Stokes Computations of the NASA Juncture Flow Model Using FUN3D and OVERFLOW (Invited)," AIAA Paper 2020–1304, doi: https://doi.org/10.2514/6.2020-1304.

[14] Lee, H.C., Pulliam, T.H., "Overflow Juncture Flow Computations Compared with Experimental Data," AIAA Paper 2019–0080, doi: https://doi.org/10.2514/6.2019-0080.

[15] Abdol-Hamid, K.S., Ahmad, N.N., Carlson, J.-R., Biedron, R.T., "Juncture Flow Computations using kL-Based Turbulence Models (Invited)," AIAA Paper 2020–1305, doi: https://doi.org/10.2514/6.2020-1305.

[16] Biedron, R.T., Lee-Rausch, E.M., "Rotor Airloads Prediction Using Unstructured Meshes and Loose CFD/CSD Coupling," AIAA Paper 2008–7341, doi: https://doi.org/10.2514/6.2008-7341.

[17] Carlson, J.-R., "Automated Boundary Conditions for Wind Tunnel Simulations," National Aeronautics and Space Administration, NASA/TM–2018–219812, 2018.

[18] Biedron, R.T., Carlson, J.-R., Derlaga, J.M., Gnoffo, P.A., Hammond, D.P., Jones, W.T., Kleb, B., Lee-Rausch, E.M., Nielsen, E.J., Park, M.A., Rumsey, C.L., Thomas, J.L., Thompson, K.B., Wood, W.A., "FUN3D Manual: 13.5," National Aeronautics and Space Administration, 2019, NASA/TM–2019–220271.

[19] Anderson, W.K., Bonhaus, D.L., "An Implicit Upwind Algorithm for Computing Turbulent Flows on Unstructured Grids," *Computers and Fluids*, Vol. 23, 1994, pp. 1–22, doi: https://doi.org/10.1016/0045-7930(94)90023-X.

[20] Biedron, R.T., Thomas, J.L., "Recent Enhancements to the FUN3D Flow Solver for Moving-Mesh Applications," AIAA Paper 2009–1360, doi: https://doi.org/10.2514/6.2009-1360.

[21] Pirzadeh, S., "Progress Toward a User-Oriented Unstructured Viscous Grid Generator," AIAA Paper 1996–0031, doi: https://doi.org/10.2514/6.1996-31.

[22] Roe, P.L., "Approximate Riemann Solvers, Parameter Vectors, and Difference Schemes," *Journal of Computational Physics*, Vol. 43, 1981, pp.357–372, doi: https://doi.org/10.1016/0021-9991(81)90128-5.

[23] Spalart, P.R., Allmaras, S.R., "A One-Equation Turbulence Model for Aerodynamic Flows," *Recherche Aerospatiale*, No. 1, 1994, pp. 5-21.

[24] Shur, M.L., Strelets, M.K., Travin, A.K., Spalart, P.R., "Turbulence Modeling in Rotating and Curved Channels: Assessing the Spalart-Shur Correction," *AIAA Journal*, Vol. 38, 2000, pp. 784–792, doi: https://doi.org/10.2514/2.1058.

[25] Spalart, P.R., "Strategies for turbulence modelling and simulations," *International Journal of Heat and Fluid Flow*, Vol. 21, 2000, pp. 252–263, doi: https://doi.org/10.1016/S0142-727X(00)00007-2.

[26] Noack, R.W., "SUGGAR: A General Capability for Moving Body Overset Grid Assembly," AIAA Paper 2005–5117, doi: https://doi.org/10.2514/6.2005-5117.

[27] Rumsey, C.L, Carlson, J.-R., Pulliam, T.H., Spalart, P.R., "Improvements to the Quadratic Constitutive Relation Based on NASA Juncture Flow Data," *AIAA Journal*, Vol. 58, 2020, pp. 4374–4384, doi: https://doi.org/10.2514/1.J059683.